

Impact of Topographic Wind Conditions on Dust Particle Size Distribution: Insights from a Regional Dust Reanalysis Dataset

Xinyue Huang¹, Wenyu Gao², Hosein Foroutan¹

¹Department of Civil and Environmental Engineering, Virginia Tech, Blacksburg, VA, 24060, USA

² Department of Mathematics and Statistics, University of North Carolina at Charlotte, Charlotte, NC, 28223, USA

Correspondence to: Hosein Foroutan (hosein@vt.edu)

Abstract. The size of windblown dust particles plays a critical role in determining their geochemical and climate impacts. This study investigates the relationship between topographic wind conditions (speed and direction relative to land slope) and the particle size distribution of dust emissions on a regional scale. We used the Multiscale Online Nonhydrostatic Atmosphere Chemistry (MONARCH) dust reanalysis dataset, which assimilates satellite data on coarse-mode dust optical depth (DOD_{coarse}). Validation against flight measurements from the 2011 Fennec campaign confirms the reanalysis's effectiveness in capturing coarse to super coarse dust. A 10-year dust reanalysis underwent selective screening to identify events with fresh emissions and the fraction of coarse dust concentrations was calculated as a surrogate for size distribution. The coarse fractions and associated meteorological and land characteristics obtained from various datasets were incorporated into multiple linear regression and machine learning models. Results indicate that dust particle size increases with wind speed, likely due to a higher fraction of fresh emissions and reduced deposition of coarse dust under stronger winds. A positive correlation between dust size and uphill slope suggests that enhanced vertical transport of dust by topography outweighs the impact of shifting emission microphysics over veering winds. Both positive correlations weaken in the afternoons and summer, likely due to the turbulence during haboob storms, which can suspend coarse dust from aged emissions, competing with the effect of uphill slopes. These findings on dust size dependency on topographic winds could improve [representation of dust cycle representation](#) and its impacts.

24

25 1 Introduction

Windblown dust particles emitted from arid and semi-arid areas are the largest terrestrial contributor to global aerosols (Brasseur and Jacob, 2017). Understanding the size of the airborne dust particles is crucial for assessing their impacts on global climate and biogeochemistry. Size plays an important role in determining the emission and deposition of dust particles and thus the redistribution of soil nutrients around the globe (Knippertz, 2017; Duce and Tindale, 1991; Wang et al., 2023). Additionally, particle size can affect the likelihood of microorganisms' attachment to dust aerosols (Polymenakou et al., 2008; Yamaguchi et al., 2012) and the distance these associated microorganisms can travel (Prospero et al., 2005; Kellogg and Griffin, 2006). Particle size, along with other factors such as mineralogy, chemical composition, and shape, controls the climate impacts of dust particles which can vary drastically from warming to cooling (Adebiyi and Kok, 2020; Kok et al., 2023; Mahowald et al., 2014). Realistic representation of dust particle size distribution (PSD) in the atmosphere requires an understanding of the dependencies of dust size at emission (Kok, 2011; Rosenberg et al., 2014).

Relationships between dust PSD and various environmental factors have been extensively studied. Soil moisture has been widely reported to increase the proportion of coarse dust in emissions by enhancing bonding forces among fine particles within soil aggregates (Dupont, 2022; González-Flórez et al., 2023; Shao et al., 2020), but one recent study also argues that the effect is non-

39 monotonic (Ma et al., 2023). Another surface characteristic of interest is soil texture. Emitted dust PSD during wind tunnel
40 experiments was reported to be significantly influenced by the fully dispersed soil size distribution (Wang et al., 2021), and
41 proportion of emitted submicron particles and PM₁₀ increased after tillage practices which broke down soil aggregates (Fernandes
42 et al., 2023; Katra, 2020). The effect of atmospheric stability on dust size is inconsistent across studies. Some reported that an
43 unstable atmospheric boundary is associated with richer submicron particles (Khalfallah et al., 2020; Shao et al., 2020), whereas
44 others found no effect (Dupont, 2022; González-Flórez et al., 2023). Deposition impacts are universally acknowledged and were
45 evaluated using characteristics of dust events or dust measurements, including fetch length (González-Flórez et al., 2023), dust age
46 (Dupont et al., 2015; Ryder et al., 2013), and dust measurement height (Khalfallah et al., 2020; Shao et al., 2020). Nevertheless,
47 the effects of multiple factors often intertwine during dust events, making the overall impact on dust size obscure.

48 Wind speed, or the resulting friction velocity (u_*) exerted on the ground surface, as the driving force of dust emissions, is one of
49 the most essential parameters for dust emissions. The relationship between wind speed and PSD of dust emissions has been widely
50 studied, yet consensus is lacking. Saltation-bombardment and aggregate disintegration are usually considered the primary
51 mechanism for dust emissions (Kok et al., 2012). Parametrization of saltation-bombardment proposed that higher u_* leads to higher
52 energy in saltating particles and thus enhances the breaking down of soil aggregates and ejection of fine particles (Shao, 2001).
53 This theory is supported by multiple wind tunnel experiments (Alfaro et al., 2022; Wang et al., 2021) and field measurements
54 (Chkhetiani et al., 2021; Dupont, 2022; Khalfallah et al., 2020). The brittle fragmentation theory, on the other hand, postulates that
55 PSD of vertical dust flux is independent of u_* , backed by compiled data from multiple wind tunnel and field measurements (Kok,
56 2011). Some also proposed that detachment of submicron particles from the surface of soil aggregates is more common when
57 kinetic energy of impacting particles is low and the ejection of ~~coaster~~ coarser particle from fragmentation becomes increasingly
58 dominant with higher impaction intensity (Malinovskaya et al., 2021). These discrepancies are partially due to the interplay of
59 other factors, such as inconsistencies in dust emission measurements (Khalfallah et al., 2020; Shao et al., 2020), soil moisture
60 (Ishizuka et al., 2008; Shao et al., 2020; Webb et al., 2021), and whether steady state saltation is reached (Mahowald et al., 2014).
61 Selection of the dust emission properties (e.g., dust flux or dust concentration; Shao et al., 2020) and the height of dust
62 measurements (Khalfallah et al., 2020) can alter the dust PSD. The effects of soil moisture on shifting dust PSD at emission can
63 get entangled with the potential effects of u_* . For instance, the fine fraction in dust emissions counterintuitively increasing with
64 decreasing u_* after light rain was caused by drying of the weakly crusted soils over time (Shao et al., 2020). With interferences of
65 various factors, predicting the general dependency of PSD of dust emission on u_* at regional scales over longer time becomes
66 complex.

67 The role of topography in altering size of dust emission is of emerging interest. The orographic channelling of winds can affect the
68 dust emission or transport (Caton Harrison et al., 2021; Rosenberg et al., 2014). Uphill winds can enhance the vertical transport of
69 dust particles through flow separation, especially increase the proportion of coarse particles in the elevated dust based on
70 computational simulations (Heisel et al., 2021). Moreover, the veering angle between wind vectors and the surface inclination can
71 affect the emitted dust PSD. A study over a local field observed that compared to winds that blew more parallel to the ridges of
72 the slopes (i.e., tangential winds), frontal uphill winds generated a higher fraction of fine particles (0.2-2 μm) because of more
73 sputtering of fine particles on the windward slope due to resistance from the secondary aeolian structures, as well as less generation
74 of coarse particles (2-5 μm) on the leeward slope with the recirculation zone (Malinovskaya et al., 2021). Other potential
75 topographic impacts include the generation of erodible material by certain orographic winds (Washington et al., 2006) and the
76 triggering of convective storms by mountains (Knippertz et al., 2007). However, their associations with dust PSD are understudied.
77 Overall, it remains unclear whether the observed effects of wind over local topography on the PSD of dust emissions is detectable
78 at regional scales ~~and what the overall relationship between topography and dust PSD will be.~~

79 Understanding the relationship between topographic wind conditions and PSD of dust emission on a -regional scale is important
80 for simulating dust activities and impacts in atmospheric or climate models. Complementing the accumulating field data on PSD
81 of dust emissions (Shao et al., 2020; González-Flórez et al., 2023; Fernandes et al., 2023), this study aims to explore the impacts
82 of topographic wind conditions on dust PSD on a regional scale through data analysis. The regional scale means that the dust
83 emission of concern inevitably includes near-source transport and deposition. Here, we selected “fresh” dust emission events from
84 the Multiscale Online Nonhydrostatic AtmosphRe Chemistry model (MONARCH) dust reanalysis data (Di Tomaso et al., 2022)
85 and constructed models to investigate the correlations between PSD of surface dust concentrations in fresh emissions and wind
86 conditions over slopes, while taking into account other relevant meteorological and surface conditions. Our methodology,
87 sensitivity analysis, and evaluations are described in Section 2, and the discussion of our findings followed by the main takeaways
88 are presented in Sections 3 and 4.

89

90 **2 Data and Methods**

91 **2.1 Datasets and variables**

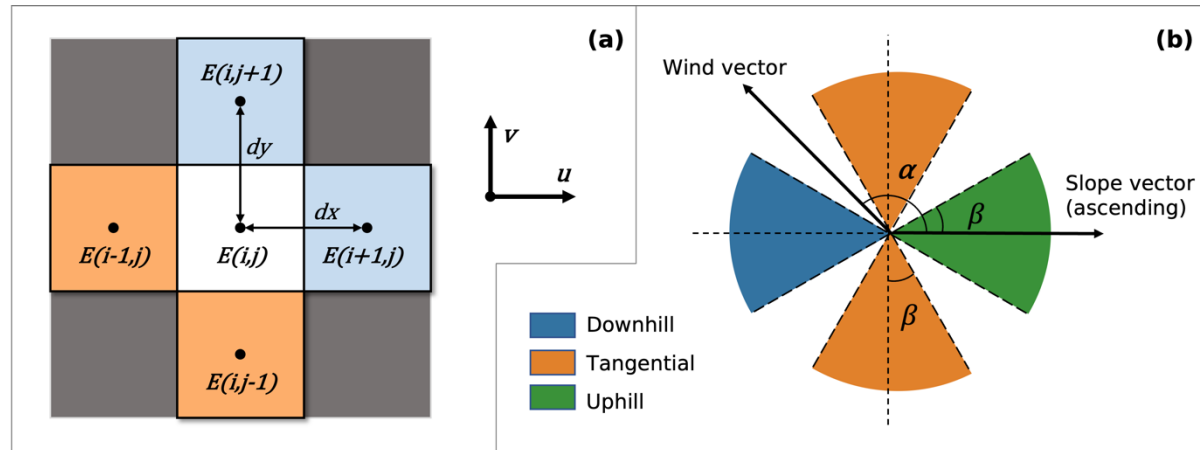
92 The study domain (12-38° N, 18W-36° E) encompasses the Sahara Desert, the largest dust source on Earth, which contributes to
93 around 60% of the global dust loading (Tanaka and Chiba, 2006). Various monitoring or reanalysis datasets are available for this
94 region, providing information on African dust sizes and the associated environmental conditions needed for this study.

95 The Multiscale Online Nonhydrostatic AtmosphRe Chemistry model (MONARCH) dust reanalysis (Di Tomaso et al., 2022)
96 dataset provides size-resolved dust information from 2007 to 2016 with 3-hour intervals. The dataset covers North Africa, the
97 Middle East, and Europe using a rotated-pole projection with a spatial resolution of 0.1°. The assimilation data of coarse-mode
98 dust optical depth (DOD_{coarse}) were derived from the Moderate Resolution Imaging Spectroradiometer (MODIS)-Aqua Deep Blue
99 level 2 aerosol products (Collection 6), including aerosol optical depth (AOD), the Ångström exponent, and the single scattering
100 albedo at different wavelengths (Ginoux et al., 2012; Pu and Ginoux, 2016). MONARCH’s first-guess dust size distribution follows
101 the brittle-fragmentation theory of Kok (2011) with perturbations across 12 ensemble members. By applying a local ensemble
102 transform Kalman filter with four-dimensional extension (4D-LETKF) at each 24-hour assimilation window, reanalysis increments
103 were added to the model ensemble simulations (first-guess) to match the DOD_{coarse} observations. Specifically, the dust state vector
104 of the total coarse dust mixing ratio (distributed across five coarser bins from 1.2 to 20 μm) was updated, then the increments for
105 the finer three bins were determined proportionally to their total relative mass. Therefore, although MONARCH reanalysis does
106 not directly assimilate fine-mode DOD, corrections in the coarse bins propagated to the entire PSD through the assimilation state
107 vector and physical parameterizations, aligning the PSD more closely with dust-specific observations. Consequently, if the prior
108 PSD is biased—for instance by placing too much mass in the largest bin or not enough in a medium bin—that bias may persist to
109 some extent after assimilation. Despite the limitation, validation against AERONET data indicates that fine dust is still captured
110 satisfactorily (Di Tomaso et al., 2021; Mytilinaios et al., 2023), supporting the reliability of the dataset to investigate dust PSD.
111 We hypothesize that the dust concentration reanalysis captures the potential regional effects of topographic wind conditions on the
112 dust PSD via assimilation of the satellite DOD_{coarse} observations. The adjustments in dust concentration PSD during data
113 assimilation were showcased by the uneven ratio of the first-guess dust concentration to its reanalysis across eight size bins (see
114 section 2.2 and Fig. S1). The MONARCH model was run in 40 hybrid pressure-sigma model layers and the dust concentration in
115 the lowest layer is saved as the surface dust concentration. The surface dust concentration best represents near-source dust

116 emissions and transport, and was chosen for this study. The concentration is available in eight size bins (i.e., 0.2–0.36, 0.36–0.6, 117 0.6–1.2, 1.2–2.0, 2.0–3.6, 3.6–6.0, 6.0–12.0, and 12.0–20.0 μm ; Klose et al., 2021)). For easier comparison, these size-resolved 118 concentrations were condensed into a single index called the “coarse fraction”, defined as the sum of mass concentrations of the 119 coarsest two bins (6–12 μm) divided by the total mass concentration of all eight bins (referred to as “cf2”). The delineation of fine 120 and coarse particles is somewhat arbitrary and case-specific across studies. In general, a cutoff diameter from submicron to above 121 10 μm was used (Dupont, 2022; Fernandes et al., 2023; Panebianco et al., 2023) and the most common range is roughly 2–5 μm 122 (Ishizuka et al., 2008; Ryder et al., 2019; Shao et al., 2020; Webb et al., 2021), which generally aligns with the lower boundary of 123 6 μm used in this study. Additionally, we tested alternative definitions of coarse fraction (namely “cf1” and “cf3”, where the 124 coarsest one or three bins are assigned as coarse dust) in the subsequent statistical analysis and results suggest that cf2 is a 125 representative surrogate for dust particle size. More details on the comparison are included in Table S4 and Section 3.3.

126 Because wind conditions associated with dust concentrations are not available from the MONARCH dust reanalysis dataset, we 127 sourced the information from the Modern-Era Retrospective analysis for Research and Applications (MERRA-2) data (Gelaro et 128 al., 2017). MONARCH ensemble simulations applied meteorological inputs from two reanalysis datasets, i.e., MERRA-2 and 129 ERA-Interim. Given that wind from both reanalyses are highly constrained by observations, and there is a substantial overlap in 130 the assimilated data used by the two (Fujiwara et al., 2024; Rienecker et al., 2008; Dee et al., 2011; Gelaro et al., 2017), it is 131 reasonable to use MERRA-2 wind vectors to inform the wind conditions of MONARCH dust reanalysis. The available wind 132 components nearest to the surface and most relevant to dust emissions are at 2 meters above ground, provided as hourly average 133 with a spatial resolution of 0.5° latitude \times 0.625° longitude in the product M2I1NXASM. Wind speed and wind direction are 134 subsequently calculated.

135



136
137 **Figure 1.** (a) Variables used in the calculation of upwind slope. The elevations in the target grid, $E(i,j)$ and the upwind grids (in orange if the 138 wind components were positive; in light blue if the wind components were negative) were used to calculate the upwind slope components in x 139 and y directions. (b) Methods for assigning the type of wind direction over topography. The angle between the upwind slope and the wind vector, 140 α , and the predefined cut-off angle, β , together determine whether the wind from an event is typical for any of the three categories of relative 141 wind direction, namely downhill, tangential, and uphill winds.

142

143 The wind direction types relative to topography (hereafter “relative wind direction type”) were determined based on the angle, α 144 ($0 \leq \alpha < 360^\circ$) between the wind vector ($u(i,j)$ and $v(i,j)$) and the slope vector ($S_x(i,j)$ and $S_y(i,j)$). Elevation data for calculating the 145 slope were retrieved from the NASA Shuttle Radar Topography Mission Global 3 arc-second (SRTM GL3) dataset (Farr et al., 146 2007). The SRTM elevation data are expected to be compatible with the MERRA-2 wind reanalysis because 1) both the SRTM

147 and GTOPO30, which is used in the Goddard Earth Observing System (GEOS-5) model (MERRA-2's first-guess), have much
 148 finer than MERRA-2's grid, making their spatially averages comparable, and 2) MERRA-2 wind reanalysis are highly constrained
 149 by assimilated observations, reducing its dependency on topographic input. Dust concentration is most relevant to emissions in
 150 upwind grids, therefore, slope vector components in each grid (i,j) were determined as gradients of elevation between the target
 151 grid and the two neighboring grids in the upwind directions (Fig. 1(a) & Eq. (1)). To the best of the authors' knowledge, this study
 152 presents the first derivation of the upwind slope over North Africa.

153 The wind direction over topography was categorized into tangential, uphill, and downhill winds depending on the angle α between
 154 the slope and wind vectors as well as a predefined cut-off angle, β ($0 < \beta \leq 45^\circ$) (Fig. 1(b) & Eq. (2)). A smaller cut-off angle
 155 results in a more selective process for assigning the relative wind direction types.

156

$$157 \quad S_x(i,j) = \begin{cases} \frac{E(i,j) - E(i-1,j)}{dx}, & u(i,j) > 0 \\ \frac{E(i,j) - E(i+1,j)}{dx}, & u(i,j) < 0 \end{cases}, \quad S_y(i,j) = \begin{cases} \frac{E(i,j) - E(i,j-1)}{dy}, & v(i,j) > 0 \\ \frac{E(i,j) - E(i,j+1)}{dy}, & v(i,j) < 0 \end{cases}, \quad (1)$$

158

159 where (i,j) denotes the location of a grid cell, $E(i,j)$ represents the elevation, and $S_x(i,j)$ and $S_y(i,j)$ represent the slope components
 160 in x and y directions, respectively. The $u(i,j)$ and $v(i,j)$ are horizontal wind components.

$$161 \quad \text{wind type} = \begin{cases} \text{uphill,} & 0 < \alpha < \beta \text{ or } (360^\circ - \beta) < \alpha < 360^\circ \\ \text{tangential,} & (90^\circ - \beta) < \alpha < (90^\circ + \beta) \text{ or } (270^\circ - \beta) < \alpha < (270^\circ + \beta), \\ \text{downhill,} & (180^\circ - \beta) < \alpha < (180^\circ + \beta) \end{cases}, \quad (2)$$

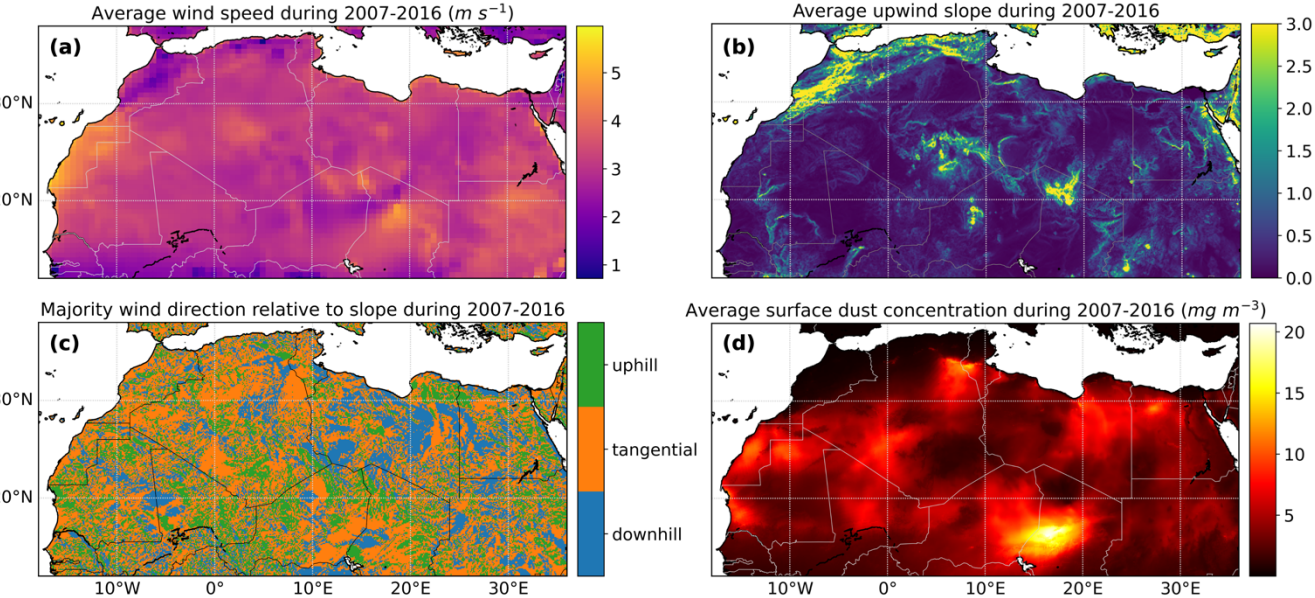
162

163 The land characteristics of soil texture and soil moisture that are expected to cast impacts on PSD of dust emissions were
 164 considered. Spatial distribution of soil texture was adopted from the map used in the Global Land Data Assimilation System version
 165 2 (GLDAS2) Noah land surface model (Rodell et al., 2004), derived from the global soil dataset by Reynolds et al. (2000). The
 166 texture of the top layer of soil was categorized into the 16 classes developed by the Food and Agricultural Organization (FAO),
 167 varying in sand, silt, and clay fractions (Jahn et al., 2006). Soil moisture data were retrieved from the MERRA-2 product
 168 M2T1NXLND, providing average water content in the top 5-centimeter layer of soil hourly with a spatial resolution of 0.5° latitude
 169 $\times 0.625^\circ$ longitude.

170 All datasets were co-registered onto a universal 0.1° Plate Carrée coordinate. MERRA-2 and MONARCH data were regridded
 171 using the Python xesmf package version 0.7.1 (Zhuang et al., 2023). The 2 m wind vectors and the soil moisture from the MERRA-
 172 2 reanalysis underwent upsampling using the "nearest source to destination" algorithm to match MONARCH's finer resolution.
 173 This algorithm does not bring in artificial variations so is the safest choice for regridding. Coarser spatial resolution of the MERRA-
 174 2 data means some neighboring grids will inevitably share the same wind vector and soil moisture, diminishing the potential effects
 175 of wind conditions on dust PSD. The SRTM elevation data with a much higher original resolution were downsampled using the
 176 "average" method provided by the Python package of geowombat version 2.1.6 (Graesser, 2023). Sub-grid information on
 177 topography was lost, but handling topography information at the same scale as the wind data is reasonable because the terrain
 178 variations at finer resolution are deemed smooth when scaling up. Soil texture data at 0.25° lat-lon coordinates were also projected
 179 to the 0.1° coordinates. To match the instantaneous 3-hourly timesteps of the MONARCH reanalysis, we picked the average wind
 180 components and soil moisture from the precedent hour, relevant to the initial dust emissions that can remain airborne during that

181 period. Maps showing the average wind speed, the average upwind slope, the most common wind direction types, and the average
 182 surface dust concentration at 0.1° resolution over the 10 years are presented in Fig. 2. While we acknowledge the inherent resolution
 183 limitations of reanalysis datasets, the focus of this study is on the broader-scale modulation of dust emission by wind conditions,
 184 and data assimilation combined with upsampling ~~techniques~~[techniques](#) ensure that our conclusion remain interpretable in this
 185 context.

186



187

188 **Figure 2.** General spatial patterns of (a) 2-m wind speed from the MERRA-2 reanalysis, (b) calculated upwind slope, (c) derived wind direction
 189 type relative to slope using cut-off angle of 10° , and (d) MONARCH total dust concentration at ground surface from 2007 to 2016. The average
 190 values are shown for wind speed, upwind slope, and dust surface concentration, and the most frequent types are shown for the relative wind
 191 direction.

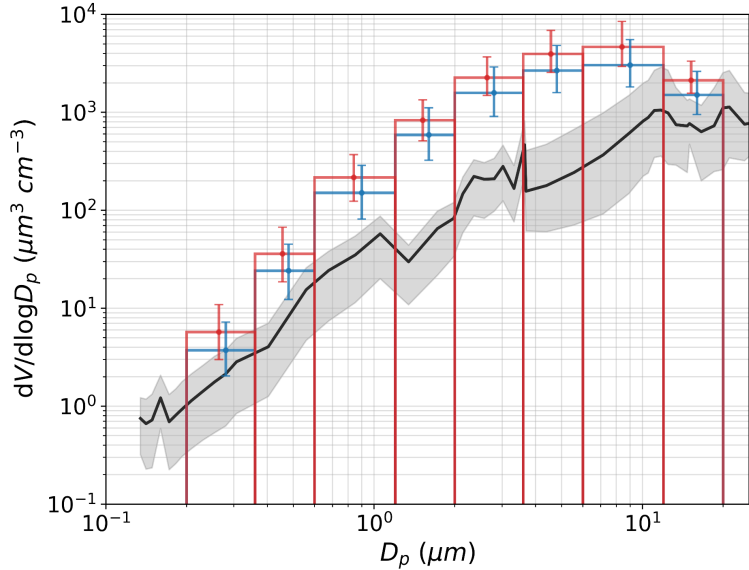
192

193 2.2 Validation against the Fennec measurements

194 The MONARCH dust reanalysis dataset was previously evaluated against observations from the Aerosol Robotic Network
 195 (AERONET) retrievals (Di Tomaso et al., 2021; Mytillinaios et al., 2023). Comparison between the 3-hourly MONARCH
 196 reanalysis of DOD_{coarse} at 550 nm and the coarse-mode AOD at 500 nm from AERONET retrievals over Sahara generate a Pearson
 197 correlation of 0.81 with a root mean square error of 0.15 (Di Tomaso et al., 2022). Here, we present an additional case study to
 198 particularly evaluate the performance of dust reanalysis on capturing fresh dust emissions. Observational data were obtained from
 199 the 2011 Fennec campaign, where size-resolved dust emissions over western Africa were intensively sampled using wing-mounted
 200 instruments (Ryder et al., 2013). Segments of three flights (b600–602), each lasted 10 minutes, over northern Mali on 17–18 June
 201 2011, were identified to be associated with fresh dust uplifts by low-level jets (Ryder et al., 2013; Ryder et al., 2015). Measured
 202 dust number concentration during these flight segments was converted to volumetric concentration for easier comparison with the
 203 MONARCH reanalysis data. The MONARCH reanalysis grids containing any portion of these flight trajectories were identified,
 204 and the associated dust mass concentrations were retrieved. These concentrations were weighted averaged by flight duration in
 205 each grid cell to yield an overall binned dust concentration. The MONARCH dust mass concentrations were also converted into
 206 volumetric concentrations using the dust particle density of 2500 kg m^{-3} for the finer four bins and $2,650 \text{ kg m}^{-3}$ for the coarser
 207 four bins (Klose et al., 2021). As shown in Fig. 3, the trends of two dust PSDs generally agree well across all the eight size bins of

208 the MONARCH dataset. Most notably, MONARCH reanalysis is effective at capturing the coarse to super coarse modes (defined
 209 as dust with diameter greater than 10 μm ; Meng et al., 2022) represented by the last three bins (3.6–20 μm), outperforming several
 210 recent dust simulations that lack the data assimilation (Adebiyi and Kok, 2020; Meng et al., 2022). Additional investigations (see
 211 Fig. S1) revealed that the reanalysis dust concentration changes non-monotonically from its first-guess, leading to the conclusion
 212 that not only the total dust concentration but also its PSD has changed due to assimilation. Overall, the predicted concentration for
 213 fresh emitted dust lies in an acceptable range, and the data assimilation process improved concentration across all bins as well as
 214 adjusted the dust size distribution, suggesting that the MONARCH reanalysis reasonably represents fresh dust emissions.

215



216
 217 **Figure 3.** The black line shows the average volumetric concentration ($\mu\text{m}^3 \text{ cm}^{-3}$) of dust sampled during three Fennec flights (6 flight segments)
 218 and the grey shaded area denotes the range of values. The blue bars show the volumetric concentration ($\mu\text{m}^3 \text{ cm}^{-3}$) of dust in corresponding grids
 219 from the MONARCH reanalysis calculated from the weighted average mass concentration, with a particle density of 2,500 kg m^{-3} for the finer
 220 four bins and 2,650 kg m^{-3} for the coarser four bins. The error bars denote the range of values.

221

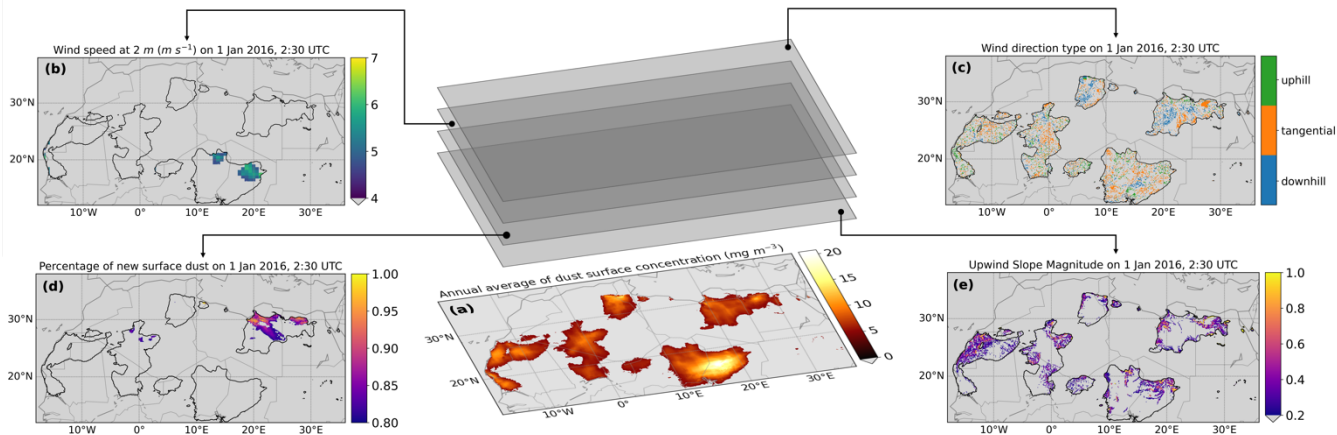
222 2.3 Event selection and sensitivity tests

223 Addressing the specific goals of this study requires the selection of the most relevant dust events from a decade of data over
 224 northern Africa. Two goals guided the screening process: 1) excluding the aged dust, and 2) focusing on wind conditions over
 225 distinctive terrain variations. Several screening criteria were accordingly developed that must be met simultaneously for dust events
 226 to be eligible for further analysis. Specifically, the selected dust events must occur within dust sources and over terrain with
 227 prominent slopes, be concurrent with high wind speeds and typical wind directions over slope, and have notable increases in dust
 228 surface concentrations. The procedures for screening these events are illustrated in Fig. 4 and described below in detail. This highly
 229 selective approach was made possible by the abundance of data from the MONARCH reanalysis.

230 To start with, dust events were confined to dust sources to exclude long-range transported and likely aged dust far from dust-source
 231 regions. The 10-year average of surface dust concentrations was calculated for the entire study domain, and pixels with values
 232 above the threshold percentile were designated as dust sources. For example, dust sources selected using the 80th percentile of the
 233 10-year average dust concentration as the threshold are presented in Fig. 4(a). The map of dust sources features the Bodélé

234 Depression, Great Sand Sea, Tanezrouft, and the Atlantic Coastal Desert, consistent with the dust sources identified in other studies
235 (Formenti et al., 2011; Di Tomaso et al., 2022). Further screening steps were performed independently within these dust sources.

236



237
238 **Figure 4.** Schematics showing the procedures for screening the 10-year dust reanalysis data for fresh dust emissions. First, dust sources were
239 assigned to regions where the annual average of dust surface concentration is among the top percentile (i.e., 20% as shown in (a)) of all values
240 across the study domain of North Africa. Subsequently, additional screening criteria were applied simultaneously to events that occurred within
241 these dust sources. These criteria include (b) high wind speed, (c) wind direction over topography, (d) high increase in dust surface concentration,
242 and (e) steep slope. Maps (b–e) are examples of filters used in the “initial” run (see in Table 1) for 1 January 2016, at 2:30 UTC.

243

244 To maximize the likelihood of capturing predominantly fresh dust emissions, high wind speed was a necessary criterion, as low
245 wind speeds are unlikely to generate sufficient fresh dust. A single cut-off value for high wind speed was chosen as a top percentile
246 of the 10-year average wind speed over the whole domain. Similarly, a single threshold slope was used to select the events over
247 prominent terrain variations. Dust events occurring over relative flat surfaces were excluded to magnify the potential signals of
248 shifted PSD due to terrain variation. Wind direction over slopes was categorized following procedures described in Section 2.1
249 and a cut-off angle smaller than 45° was used to exclusively select typical uphill, tangential, or downhill winds over slopes. Another
250 criterion for increasing the probability of capturing dominantly fresh emissions was identifying sharp increases in surface
251 concentrations. This approach favored the initiation of significant dust emissions with relative clean background dust levels.
252 Examples of selected dust events based on each of the above criteria at 2:30 UTC on 1 January 2016, are provided in Fig. 4(b–e),
253 using the configurations for the “initial” run (i.e., a cut-off angle of 10° for categorization of wind direction, the 80th percentile as
254 threshold for high wind speeds and steep slope, and 80% as the threshold ratio of the increased surface dust concentration to the
255 total dust concentration as shown in Table 1).

256 We performed several sensitivity tests to account for the uncertainties associated with the criteria used for event selection. We
257 perturbed each of the threshold percentiles or the cut-off values used in the “initial” run in a pair of sensitivity runs. Specifically,
258 we added and subtracted 10% from the threshold percentiles of 80% used for screening dust sources, steep slope, high wind speed,
259 and high fraction of fresh emissions. Cut-off angles, β of 5° and 20° were tested compared to the initial 10° for typical wind
260 direction. Configurations of all the sensitivity runs are shown in Table 1. A combination of all the stricter criteria was used in the
261 “final” run.

262

263 **Table 1.** Thresholds or cut-off values used in all runs. Locations where the 10-year average surface dust concentration is above the threshold
264 percentile value of all locations were designated as dust sources. Events over dust sources with slope and wind speed above the threshold
265 percentiles of temporally averaged values over the whole domain, and increases in dust surface concentration above the threshold values were

selected. The wind direction relative to topography was assigned using the cut-off angle. Values marked in bold represent the different criteria compared to the “initial” run.

Test name	Dust sources threshold percentile	Wind direction cut-off angle	Slope threshold percentile	Wind speed threshold percentile	Increase in dust surface concentration threshold
Initial	80	10°	80	80	80%
90%source	90	10°	80	80	80%
70%source	70	10°	80	80	80%
5cutoff	80	5°	80	80	80%
20cutoff	80	20°	80	80	80%
90%slope	80	10°	90	80	80%
70%slope	80	10°	70	80	80%
90%wdsp	80	10°	80	90	80%
70%wdsp	80	10°	80	70	80%
90%scconc	80	10°	80	80	90%
70%scconc	80	10°	80	80	70%
Final	90	5°	90	90	90%

269

2.4 Statistical analysis

270 Based on the selected events for “fresh” dust emissions, we explored the relationships between wind conditions and the PSD of
 271 emitted dust, taking into consideration the effects of various meteorological and landscape factors. Specifically, the dependent
 272 variable was the coarse fraction of surface dust, and the independent variables of focus were the wind speed and the slope associated
 273 with uphill, tangential, and downhill winds. The five additional independent variables are environmental variables that can
 274 potentially affect dust PSD as well as the relationships between dust PSD and wind conditions, including the continuous variables
 275 of year and soil moisture, and the categorical variables of time of day, season, and soil texture type. Dust events with missing
 276 values in soil texture class or wind direction type were excluded.

277 Exploratory data analysis was first conducted to assess data quality, identify intrinsic patterns, and guide the selection of
 278 appropriate statistical models. We selected and modified our statistical models based on their adherence to model assumptions,
 279 ability to explain the variability in the coarse fraction, and overall complexity. An initial choice was the multiple linear regression
 280 model which has the advantage of high explainability. We separated the slope by wind direction types to provide a more holistic
 281 representation of the effects of veering wind over topography. Significant coefficients for continuous variables, such as wind speed,
 282 represent the change in the coarse fraction of dust concentrations associated with a one-unit change in that corresponding
 283 independent variable. Categorical variables (e.g., time of day) are encoded as binary dummy variables, each representing a distinct
 284 category. The coefficients of these variables reflect the change in coarse fraction relative to the reference category chosen during
 285 the encoding process. Interaction terms can also be added to linear models in order to reflect the interplay between wind conditions
 286 and other factors. An interaction can be expressed as $x_m \times x_p$, where x_m is one of the four wind condition variables and x_p is one
 287 of the two additional continuous variables (i.e., year and soil moisture) or a dummy variable representing one of the three additional
 288 categorical variables (i.e., time of day, season, and soil texture). The adjustment in the coefficient for x_m due to x_p would be
 289 represented by $\beta_{mp}x_p$. A valid linear model requires linear relationships, normality of errors, constant variance (homoscedasticity),
 290 and low correlations among independent variables. Collinearity or multicollinearity among predictors can inflate standard errors
 291 and reduce the statistical significance of regression coefficients. To assess this, we calculated the Generalized Variance Inflation
 292 Factors (GVIFs) for all predictors in the linear models using the VIF function in R (R. Core Team, 2023). For categorical variables,
 293 the GVIFs were adjusted by the degrees of freedom (Df), expressed as $GVIF^{1/(2\cdot Df)}$. An adjusted GVIF of 1 (the smallest value)
 294 indicates no collinearity, while values below 5 generally suggest low and acceptable collinearity.

295 When assumptions of normality and constant variances were violated, we attempted standardization and transformations, including
296 the Box-Cox transformation (Box and Cox, 1964) and the logit transformation (Berkson, 1944), to tackle these issues. We also
297 tested weighted linear regression, also known as weighted least squares (WLS) (Kiers, 1997), which can handle non-constant
298 variance (heteroscedasticity) by assigning weights to observations. In addition, Beta regression models were implemented, which
299 are particularly useful for fractional variables that range between 0 and 1, such as the coarse fraction in this study (Douma and
300 Weedon, 2019). Beta regression has been previously applied to air quality-related health metrics within the standard unit interval
301 (Lu et al., 2021) and to particle size data with skewed distributions (Peleg, 2019).

302 Several evaluation metrics were used to compare model performance, including the root mean square error (RMSE), the mean
303 absolute error (MAE), the adjusted coefficient of determination (adjusted R^2 , which evaluates the amount of variability in the
304 coarse fraction explained by the model while penalizing model complexity). Higher adjusted R^2 , and lower RMSE or MAE values
305 suggest that more variations of the data are captured by models. We also calculated the prediction interval accuracy at the 95%
306 confidence level, defined as the proportion of observations covered by prediction intervals. The performance metrics were also
307 averaged using the 10-fold cross-validation (CV), where the dataset was randomly divided into 10 subsets, and models were trained
308 on 9 subsets and tested on the remaining subset in each iteration, with a total of 10 iterations. All statistical analyses were performed
309 using R and the relevant packages (Zeileis and Hothorn, 2002; Grün et al., 2012; Cribari-Neto and Zeileis, 2010; Fox and Weisberg,
310 2019; Venables and Ripley, 2002).

311 Moreover, we constructed machine learning models to account for the large dataset and potential non-linear relationships.
312 Categorical variables (wind direction, soil texture type, season, and time of day) were converted into dummy variables, resulting
313 in a total of 22 predictors when combined with continuous predictors (wind speed, slope, and year). We built Random Forest and
314 Extreme Gradient Boosting (XGBoost) models, both are widely used regressors (Bacanin et al., 2024; Brokamp et al., 2017; Keller
315 & Evans, 2019; Zhang et al., 2022). Though both models rely on decision trees, Random Forest aggregates multiple trees trained
316 on randomly sampled subset of data, whereas the XGBoost sequentially refines decision trees through iterative training. Model
317 hyperparameters were fine-tuned to ~~maximize~~ maximize the predictive performance, with the search grids determined based on
318 sample size, predictor count, and computational efficiency. The search grids and the optimal hyperparameter combinations are
319 listed in Table S1. As with the linear models, we assessed the accuracy of prediction interval coverage at 95% confidence level
320 through 10-fold CV. Machine learning models are known to have high prediction accuracy but can be challenging to interpret. One
321 technique to assess the contribution of individual predictors to the coarse fraction based on decision trees is the SHapley Additive
322 exPlanations (SHAP) analysis, which was performed on the optimized models. These analyses were conducted using Python
323 packages including scikit-learn (version 1.2.2; Pedregosa et al., 2011), xgboost (version 1.7.6; Chen and Guestrin, 2016), and
324 shap (version 0.44.0; Lundberg and Lee, 2017).

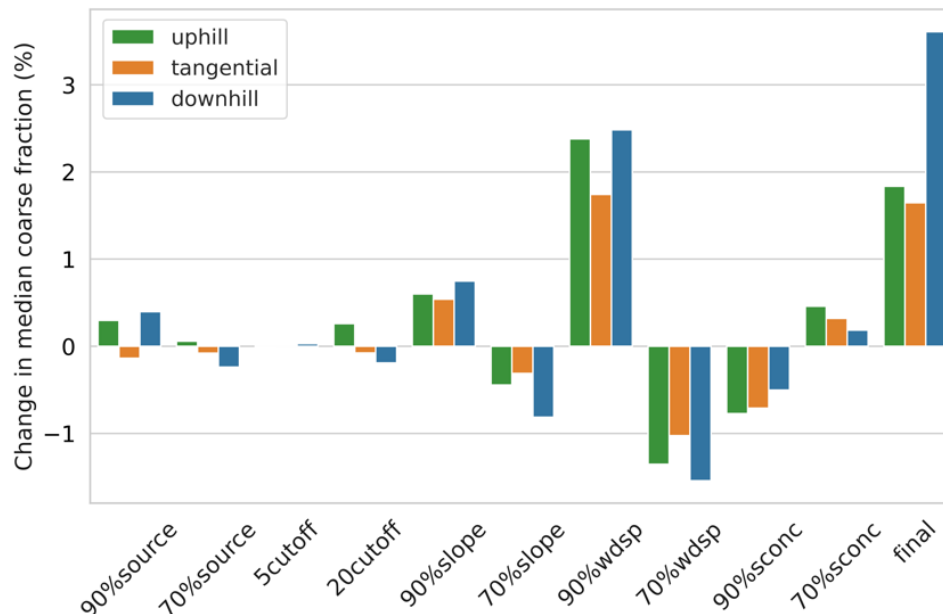
325 Eventually, the more complex models did not outperform the multiple linear models to a large extent. Given their high
326 explainability, ability to incorporate interactions between predictors, and competitive performance, we ~~ultimately~~ ultimately selected
327 linear models for further analysis. SHAP results from the machine learning models were also included for cross-validating key
328 findings. More details on the model performance and results are described in Section 3.3.

329

330 **3 Results and Discussion**331 **3.1 Sensitivity tests show minor variations**

332 As a result of the screening processes, a total number of 461,183 dust events were identified in the “initial” run and 25,884 events
 333 were identified in the “final” run from around 3.5 billion records of dust concentrations at specific locations and times. Figure 5
 334 shows the percentage changes in median coarse fraction by wind direction types from all sensitivity runs. In general, nearly all
 335 perturbations of any single screening criterion result in around $\pm 1\%$ of changes in average or median coarse fraction grouped by
 336 wind direction. The exception is restricting wind speed to the top 10% percentile (the “90%wdsp” run), which leads to a roughly
 337 2% increase in the median values for each wind direction type. Coarse fraction of dust emissions with downhill winds are usually
 338 more sensitive to the threshold values used for screening than emissions with the other two wind directions. When all criteria were
 339 restricted simultaneously in the “final” run, the median coarse fraction of dust emission increases by less than 2% under tangential
 340 or uphill winds and around 3.5% under downhill winds. Considering the minor variations in coarse fraction among sensitivity runs,
 341 we decided to focus on one run for more detailed analysis. The “final” run was chosen because, in theory, the selected events are
 342 most representative for fresh dust emissions.

343



344

345 **Figure 5.** Percentage change in the median coarse fraction by wind direction type for all sensitivity runs as compared to the “initial” run.

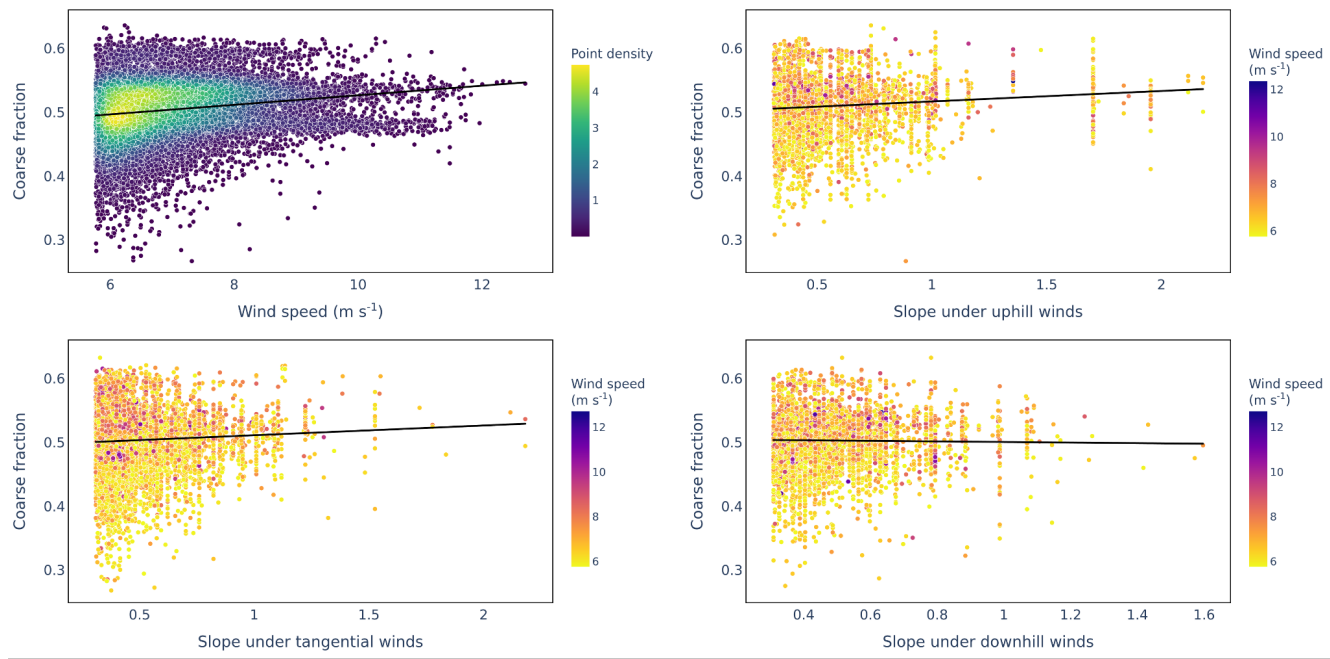
346

347 **3.2 Exploratory analysis**

348 To gain an impression of the general distribution of the data, we started with plotting the dust coarse fraction against four variables
 349 of wind conditions in Fig. 6. Scatter points in the panel for wind speed are color-coded by number of overlapping observations,
 350 and data points in other three panels for slopes are color-coded by wind speed. Across all four panels, a pattern of heteroscedasticity
 351 is revealed, that is, the variance of coarse fraction is greater for dust events associated with lower wind speed or slope than for
 352 those with high wind speed or slope. The vertically aligned scatter points with varying colors at a slope of around 1.7 in the panel
 353 for “slope under uphill winds” represent 93 dust events that occurred at a same location under different wind speeds near the
 354 northern border of Western Sahara during 2007–2016, illustrating how a larger number of dust events can lead to higher variance.

355 No obvious non-linear relationships between the four wind condition variables and the coarse fraction are observed. The trend
 356 lines based on simple linear regression models of the coarse fraction against each wind condition variable indicate general trends
 357 in the dust PSD with varying wind conditions, but the significance of these relationships is not assured. Additional plots for the
 358 soil moisture and slope under three wind conditions with color-codes representing the density of overlapping data points is
 359 presented in Fig. S2.

360
 361



362
 363 **Figure 6.** Scatter plots and linear trend lines of relationships between the coarse fraction of surface dust concentration and the wind speed and
 364 the slope under three different wind directions. In the upper left panel for wind speed, the color-codes present the number of overlapping data
 365 points. In the other three panels for slope, the color of each scatter point represents the associated wind speed for the dust event.

366

367 **3.3 General associations between wind conditions and dust coarse fraction**

368 The absence of obvious non-linear relationships between coarse fraction and wind conditions from the exploratory analysis further
 369 motivated us to initially construct linear regression models, in addition to it being a common starting point. The linear model
 370 including all independent variables but no interactions has an adjusted R^2 value of 0.224, RMSE with 10-fold CV of 0.070, and
 371 MAE with 10-fold CV of 0.059. Additionally, we added all possible interactions into the model and fine-tuned it by removing the
 372 insignificant interaction terms. The resulting model with interactions has similar performance, with the adjusted R^2 of 0.239, RMSE
 373 with 10-fold CV of 0.070, and MAE with 10-fold CV of 0.058. The somewhat weak correlations may be related to factors that are
 374 not included in the model, such as deposition, variability within the same categories of soil texture, etc. Residual analyses indicate
 375 violations of the assumptions of evenly distributed variance and normality (Fig. S3). We attempted to address these issues and
 376 improve model performance through various linear model adaptations but only obtained indefinite or marginal improvements—
 377 standardizing the coarse fraction and wind conditions variables yields an adjusted R^2 of 0.241, RMSE with 10-fold CV of 1.678,
 378 and MAE with 10-fold CV of 1.420; and logit transformation on the coarse fraction generates an adjusted R^2 of 0.237, RMSE with
 379 10-fold CV of 1.420, and MAE with 10-fold CV of 0.487. Furthermore, the Box-Cox transformation, weighted least squares
 380 (WLS), or Beta regression models with the best-performing configuration (with a log-log link function for the mean and an identity

link function for the dispersion) all failed to resolve heteroscedasticity in the residuals with respect to wind condition variables. For the machine learning models, the optimized Random Forest and XGBoost models achieved R^2 values of 0.407 and 0.474, respectively, which dropped to 0.259 and 0.273 after 10-fold CV, indicating potential overfitting. The coverage rates of prediction intervals with the 10-fold CV are 92.5% for Random Forest and 54.4% for XGBoost, both lower than the 94.0% coverage by the linear models both with and without interactions. Linear models outperforming machine learning models on prediction accuracy strongly encourages the selection of linear models. Considering their comparative satisfactory performance, simplicity, and directly interpretable coefficients, we decided to proceed with the linear regression models among all models. We first assessed the influence of individual predictors based on the linear regression model without interactions, with cross comparison with results from the machine learning models (Fig. S5). Subsequently, we used the linear model with interaction terms to investigate the effects of interactions among predictors.

Linear model without interaction terms are used to infer the general effects of wind conditions on coarse dust fraction. These linear models are not intended to imply strictly linear relationships between dust PSD and wind conditions, but rather to provide initial guidance on the directionality of these relationships. Although individual data points present deviations, our models effectively predict the overall trend, as suggested by the response vs. fitted value plots (Fig. S4), where the predicted values align closely with observed values and cluster around the one-to-one red line. Adjusted GVIF values for the model without regression were consistently below 2 with most values close to 1 (Table S2), indicating that multicollinearity among continuous or categorical predictors does not significantly affect the regression model. The multiple linear regression model for the dust coarse fraction includes four independent variables for wind conditions (speed and three options for slope) and additional factors that may affect the PSD of dust emissions, allowing us to investigate the effects of topographic wind conditions while controlling interferences from other environmental factors. The model can be expressed as:

401

$$402 \quad y = \beta_0 + \beta_1 x_1 + \beta_2 x_2 + \beta_3 x_3 + \beta_4 x_4 + \beta_5 x_5 + \beta_6 x_6 + \beta_7 x_7 + \beta_8 x_8 + \beta_9 x_9 + \epsilon, \quad (3)$$

403

404 where, y represents the coarse fraction of dust emissions, x_1 represents wind speed, and x_2 , x_3 , and x_4 represent slope under uphill, 405 tangential, and downhill winds, respectively; x_5 is the categorical variable of time of day, including three levels of morning (6:00– 406 12:00 local time), afternoon (12:00–18:00 local time), and evening (18:00–6:00 local time); x_6 is the categorical variable of season, 407 comprising DJF (winter months of December, January, and February), MAM (spring months of March, April, and May), JJA (summer months of June, July, and August), and SON (autumn months of September, October, and November); x_7 and x_8 represent 408 the continuous variables of year and soil moisture; and x_9 is the categorical variable of soil texture class, which contains eight 409 levels of the FAO soil texture classes (Jahn et al., 2006). The coefficients β_i represent the expected changes in the response variable 410 y per unit increase in the continuous predictor x_i , and the difference in y relative to the reference category for categorical predictor 411 x_i , while holding all other variables constant. The ϵ represents the residuals of the model. The default coarse fraction is cf2 (defined 412 in Section 2.1), and the corresponding estimated values, standard errors, and significance of the wind condition coefficients are 413 presented in Table 2, with full details of all coefficients in Table S3. As noted in Section 2.1, we also tested two alternative 414 definitions of coarse fraction (cf1 and cf3) and compared the estimated coefficients with their statistical significance in Table S4. 415 The coefficient estimates based on cf2 and cf3 are largely consistent, whereas those based on cf1 show some distinct patterns. 416 Given that dust in the top bin (12–20 μm) falls into the “super coarse” dust category ($> 10 \mu\text{m}$; Meng et al., 2022), these results 417

418 suggest that super coarse dust responds differently to varying wind conditions compared to other coarse dust. Therefore, the cf2
419 definition serves as a robust representation of coarse dust particles.

420 The coefficient for wind speed from the linear model is statistically significant and positive (Table 2), suggesting that controlling
421 the effects of other factors, the coarse fraction of dust emissions increases with the wind speed. This result is consistent with the
422 SHAP analyses on both machine learning models as showcased in the SHAP summary plot (Fig. S5), where purple data points
423 with high wind speed are concentrated on the right side of the vertical centerline and yellow points with lower wind speed
424 dominates the left side, indicating a positive correlation between wind speed and coarse fraction. The observed trend contradicts
425 implications of the theory based on the saltation-bombardment emission mechanism, which predicts that higher kinetic energy of
426 impact particles from greater wind speed can intensify the disintegration of soil aggregates and thus the release of finer particles
427 (Shao, 2001; Alfaro et al., 1997). Conversely, our result aligns with the observed shift in the dominant emission mechanism from
428 “shaking-off” of submicron particles to the generation of coarser microparticles from fragmentation as the velocity of saltating
429 particles increases (Malinovskaya et al., 2021). An alternative explanation for the observed positive effect of wind speed on dust
430 size at emission is related to soil conditions (Ishizuka et al., 2008; Panebianco et al., 2023). Emissions of super coarse dust (> 10
431 μm) increased with wind speed while the emissions of ultrafine dust ($< 1 \mu\text{m}$) remained nearly invariant over sandy soil
432 (Panebianco et al., 2023); in addition, the fraction of fine dust ($< 2 \mu\text{m}$) decreased with friction velocity on slightly crusted surfaces
433 (Ishizuka et al., 2008). These phenomena were likely due to weaker cohesive forces and thus easier emission for coarse particles
434 than fine particles. Though our sensitivity test using cf1 rejects the increased emission of super coarse dust with wind speed (Table
435 S4), unmeasured changes in the fine dust emissions leading to an overall higher coarse fraction remain one possibility. Soil texture
436 and soil moisture were included in the model, but subtle discrepancies across events within the same soil class or soil moisture are
437 not eliminated. Last but not least, since the fresh dust emissions at regional scale inevitably include transported dust, yet another
438 potential explanation is unrelated to the emission, but to the transport process—as wind speed increases, more fresh emissions are
439 generated, which undergo less deposition and contain a higher fraction of coarse particles than the aged background dust (González-
440 Flórez et al., 2023).

441
442 **Table 2.** Estimates, standard errors, and p-values of wind condition coefficients for the multiple linear model of dust coarse fraction. The model
443 includes the independent variables of wind conditions (i.e., wind speed and slope under three wind direction types), time of day, season, year,
444 soil moisture, and soil texture. The symbols of coefficients are defined in Eq. (3).

Coefficients for Variables	Estimates	Standard errors	p-values
wind speed (β_1)	0.0075	0.0002	<0.0001
slope with uphill winds (β_2)	0.0175	0.0013	<0.0001
slope with tangential winds (β_3)	0.0081	0.0015	<0.0001
slope with downhill winds (β_4)	0.0076	0.0016	<0.0001

445
446 The coefficients for slopes under all three wind directions from the linear regression are significant and positive (Table 2),
447 suggesting that the coarse fraction of dust emissions increases with the slope regardless of the relative wind direction. The largest
448 coefficient for uphill winds among all three slopes indicates that it has the strongest effect on dust coarse fraction. Similarly, the
449 SHAP analysis on the optimized Random Forest model (Fig. S5) suggests a positive relationship between slope and coarse fraction,
450 with uphill winds further accentuate the positive effects. The XGBoost model indicates mixed effects of wind directions but the
451 results are less reliable due to its lower prediction accuracy. Overall, the linear model and the Random Forest model agree on the
452 positive correlation between slope, ~~espacially~~especially under uphill winds, and dust size. The strong increase in coarse fraction
453 with uphill slope aligns with previous findings using large eddy simulations, which was explained by the enhancement in vertical

454 transport of dust particles being more prominent for coarser particles (Heisel et al., 2021). In contrast, the microphysics of dust
 455 emission proposed that compared to tangential winds, uphill winds against the slope resulted in more detachment of fine particles
 456 from the surface of soil aggregates on the windward slope due to the secondary aeolian structures, and meanwhile less ejection of
 457 coarse particles from the fragmentation of soil aggregates upon hitting the leeward slope (Malinovskaya et al., 2021). Our results
 458 suggest that at the regional scale, the effect of near-source transport of emitted dust at scales of hundreds to thousands of meters
 459 dominates over the impact of microphysics of dust emission related to secondary dune structure at scales of centimeter to meters.
 460 The overall elevated coarse fraction with slopes might also be attributed to the orographic wind channelling (Rosenberg et al.,
 461 2014), increased availability of coarser particles on hills (Samuel-Rosa et al., 2013; Washington et al., 2006) and their greater
 462 mobility under gravity. Effects of slope under tangential and downhill winds are less pronounced, with linear model suggesting
 463 their weaker positive relationships with coarse fraction compared to uphill winds (Table 2), and the Random Forest model
 464 indicating negative impacts of tangential and downhill wind directions on coarse fraction even though the effect of slope is positive
 465 (Fig. S5). These weaker effects can possibly be explained by the lack of effective enhancement in vertical transport of coarse
 466 particles on the windward side of slopes.

467 3.4 Associations between wind conditions and dust coarse fraction under varying environmental conditions

468 Interaction terms in the model allow us to investigate how the relationships between wind conditions and dust coarse fraction may
 469 vary depending on the additional variables for time and surface characteristics. The model including all significant interactions is
 470 shown in Eq. (4). Results for coefficients related to the interactions are shown in Table 3 and the complete results are included in
 471 Table S5.

$$472 \\ 473 y = \beta_0 + \beta_1 x_1 + \beta_2 x_2 + \beta_3 x_3 + \beta_4 x_4 + \beta_5 x_5 + \beta_6 x_6 + \beta_7 x_7 + \beta_8 x_8 + \beta_9 x_9 + \beta_{15} x_1 x_5 + \beta_{16} x_1 x_6 + \beta_{18} x_1 x_8 + \beta_{25} x_2 x_5 + \\ 474 \beta_{26} x_2 x_6 + \beta_{28} x_2 x_8 + \beta_{35} x_3 x_5 + \beta_{38} x_3 x_8 + \beta_{46} x_4 x_6 + \epsilon, \quad (4)$$

475 where, $x_1 - x_9$, y , and $\beta_1 - \beta_9$ are the same as in Eq. (3). The β_{ij} are coefficients for interactions between x_i ($1 \leq i \leq 4$) and
 476 x_j ($5 \leq j \leq 9$) and their interpretations are described in Section 2.4.

477 With interactions in the model, the coefficient β_{11} indicates the slope of linear correlation between wind speed and the coarse
 478 fraction when the variables that have interactions with wind speed are at the reference levels for categorical variables (i.e.,
 479 “afternoon” for time of day and “DJF” for season) or at zero for continuous variable (i.e., soil moisture). Adjustments of the
 480 correlation under other conditions are indicated by the coefficients for interactions with wind speed (β_{15} , β_{16} , and β_{18}). The overall
 481 coefficient for wind speed stays positive with varying time of day and season, except for the rare cases when soil moisture is high
 482 ($> 50\%$), which agrees with the results from the model without interactions (Table 2). As suggested by the adjustments of
 483 coefficients, the positive correlation between wind speed and coarse fraction is weakened during events that happen in the
 484 afternoon, in summer, or are associated with higher soil moisture. All these conditions are typical for haboob dust storms which
 485 are capable of generating intense dust emissions (Heinold et al., 2013; Knippertz, 2017). Therefore, a potential explanation for the
 486 observed patterns is that the dust PSD dependency on wind speed is reduced during convective conditions associated with haboobs.
 487 Reasons behind the weakened correlation could be related to turbulent atmospheric conditions. Based on the above assumption
 488 that the coarse fraction increases with wind speed due to the associated higher proportion of fresh emissions, during convective
 489 events, the role of turbulent flows in keeping dust particles suspended regardless of the magnitude of wind speed may blur the

491 effects of wind speed. Moreover, the positive relationship between wind speed and coarse fraction diminishes with soil moisture.
 492 Higher soil moisture may inhibit fresh dust emissions, which, as discussed in Section 3.3, potentially contribute to the positive
 493 correlation between wind speed and coarse dust fraction, thereby weakening the correlation.

494

495 Table 3. Estimates, standard errors, and p-values of the interaction coefficients for the multiple linear model of dust coarse fraction.
 496 The model includes the independent variables of wind conditions (i.e., wind speed and slope under three wind direction types),
 497 time of day, season, year, soil moisture, and soil texture, as well as significant interaction terms between wind conditions and other
 498 independent variables. The interaction coefficients represent wind conditions (speed and direction) under various situations of time
 499 of day, season, and soil moisture. The symbols of coefficients are defined in Eq. (3) and (4). Statistically significant (at 0.05
 500 significance level) coefficients are bolded and their p-values are marked with “**”, among which the negative coefficients are
 501 italicized.

Multiple linear model coefficients for wind speed under various conditions			
	Estimates	Standard errors	p-values
Afternoon, DJF, and soil moisture of 0 (reference levels; β_1)	0.0076	0.0007	<0.0001*
Adjustments with time of day (β_{15})			
evening	0.0122	0.0006	<0.0001*
morning	0.0016	0.0006	0.0058*
Adjustments with season (β_{16})			
JJA	-0.0028	0.0007	<0.0001*
MAM	-0.0023	0.0006	0.0003*
SON	-0.0003	0.0007	0.6500
Adjustments with soil moisture (β_{18})	-0.0154	0.0029	<0.0001*
Multiple linear model coefficients for slope with uphill winds under various conditions			
	Estimates	Standard errors	p-values
Afternoon, DJF, and soil moisture of 0 (reference levels; β_2)	0.0135	0.0030	<0.0001*
Adjustments with time of day (β_{25})			
evening	0.0061	0.0024	0.0118*
morning	0.0159	0.0026	<0.0001*
Adjustments with season (β_{26})			
JJA	-0.0098	0.0028	0.0005*
MAM	-0.0138	0.0029	<0.0001*
SON	-0.0056	0.0031	0.0672
Adjustments with soil moisture (β_{28})	0.0521	0.0107	<0.0001
Multiple linear model coefficients for slope with tangential winds under various conditions			
	Estimates	Standard errors	p-values
Afternoon, soil moisture of 0 (reference levels; β_3)	-0.0038	0.0025	0.1261
Adjustments with time of day (β_{35})			
evening	0.0134	0.0024	<0.0001*
morning	0.0110	0.0027	<0.0001*
Adjustments with soil moisture (β_{38})	0.0351	0.0115	0.0022*
Multiple linear model coefficients for slope with downhill winds under various conditions			
	Estimates	Standard errors	p-values
DJF (reference level; β_4)	0.0148	0.0026	<0.0001*
Adjustments with season (β_{46})			
JJA	-0.0101	0.0031	0.0011*
MAM	-0.0105	0.0032	0.0011*
SON	-0.0090	0.0036	0.0116*

502

503 The adjustments of the relationship between slope and coarse fraction with other environmental variables are generally consistent
504 across three wind direction types. Overall, the coefficients for slope with three wind directions stay positive under most
505 circumstances, aligning with results from the model without interactions (Table 2). Notably, the effect of the uphill slope is
506 strongest in the morning. Unlike Harmattan surges, which can induce dust emission throughout the day, or haboob storms, which
507 mostly occur in the afternoons, dust uplift due to the breakdown of night-time low-level jets (NLLJs) is limited to the period around
508 sunrise to midday (Fiedler et al., 2015; Heinold et al., 2013). Therefore, the result indicates that the role of uphill slope in facilitating
509 transport of coarse dust is particularly relevant during emissions related to NLLJs. Moreover, the effect of slope in increasing
510 coarse fraction is weakest during afternoon events under both uphill and tangential winds. With both uphill and downhill winds,
511 the positive correlation between slope and coarse fraction is the strongest in winter, and the weakest in spring and summer. The
512 reduced correlation of dust PSD with uphill slope in both afternoon and summer suggests a diminished effect of slope during
513 haboob dust storms. This can be explained by the stronger turbulence associated with convective storms, which readily stirs up the
514 air and facilitate particle transport, thereby weakening the additional effect of uphill slope by elevating coarse particles through
515 flow separation.

516 The effect of slope on increasing coarse fraction of dust also becomes more apparent with increasing soil moisture under uphill
517 and tangential winds. Low soil moisture might be associated with low water vapor content in lower-Saharan Air Layer, which can
518 lead to continued vertical motions of the atmosphere into the night due to increased atmospheric longwave heating (Ryder, 2021).
519 Conversely, the air is more stable with higher relative humidity, making the enhancement by topography more critical for the
520 transport of coarse dust.

521

522 4 Conclusion

523 This study aims to explore the relationship between topographic wind conditions and particle size distribution (PSD) of dust
524 emissions on a regional scale through data analysis. The Multiscale Online Nonhydrostatic AtmospheRe Chemistry model
525 (MONARCH) dust concentrations were first evaluated against flight measurements of fresh dust emissions from the 2011 Fennec
526 campaign and were proven to be effective in capturing concentrations of coarse to super coarse dusts in fresh dust emissions. For
527 our analysis, size-resolved surface dust mass concentrations from the MONARCH dust reanalysis over the Sahara during 2007–
528 2016 were condensed into an index of coarse fraction (the ratio of the sum of concentrations in the top two bins (6–20 μm) to the
529 total concentration in eight bins (0.2–20 μm)), serving as the proxy for size distribution. Information on wind vectors and soil
530 moisture, elevation, and soil texture was obtained from the Modern-Era Retrospective analysis for Research and Applications
531 (MERRA-2) reanalysis data, the NASA Shuttle Radar Topography Mission Global 3 arc-second (SRTM GL3) dataset, and the
532 inputs to the Global Land Data Assimilation System version 2 (GLDAS2) Noah land surface model, respectively. Several highly
533 selective criteria were applied to maximize the probability of selecting fresh dust emissions with typical wind conditions over
534 topography. Scatter plots of coarse fraction against four wind conditions variables (i.e., wind speed, slope under uphill, tangential,
535 and downhill winds) reveal unevenly distributed variance without obvious non-linear trends. We ~~ultimately~~ultimately selected the
536 multiple linear models after testing several model variations to quantify and explain the trends in data, with key findings cross-
537 validated using machine learning models.

538 The linear model without and with significant interaction terms can explain 22% and 24% of the variability of coarse fraction,
539 respectively. The model, however, fails to fulfil the assumptions on homoscedasticity (constant variance) and normality, and this

issue could not be resolved by other parametric modelling approaches including linear regression models with transformations of variables, weighted least square, or Beta regression models with several options for link functions. The strong intrinsic pattern of non-constant variance and the abundance of data points require more advanced models, which is beyond the scope of our current work. Other uncertainties arose from the varying original resolution of datasets and the resampling process. Moreover, even though we applied multiple criteria to exclusively pick fresh dust emissions, we cannot totally exclude the portion of transported dust. The analysis focuses on the general trend for North Africa, and more detailed insights rely on analysis for smaller geographic domains.

Despite some limitations, the multiple linear models achieved high predictive accuracy—over 94% under 10-fold cross-validation (CV)—demonstrating their capability to provide meaningful insights for interpretation. The optimized Random Forest model, which attained 92% predictive accuracy with 10-fold CV despite potential overfitting, ~~adding~~added insights to the influence of each predictor by applying the SHapley Additive exPlanations (SHAP) analysis. Both the linear and ~~machine learning~~the Random Forest models ~~consistently~~ reveal positive associations between coarse dust fraction and both wind speed and slope. ~~The impact of wind speed may possibly be attributed to a higher proportion of fresh emissions, or a greater resistance of surface soil to disintegration into fine dust particles. An increased coarse fraction in dust emissions with wind speed is inconsistent with theories by Kok (2011) or those based on saltation-bombardment mechanism (Shao, 2001; Alfaro et al., 1997), which predict invariant or opposite trends, respectively. The most likely explanation for our finding is that higher winds are associated with more fresh emissions (which undergo less deposition) because transported dust was inevitably included in our samples even with meticulous screening (González-Flórez et al., 2023). Therefore, our finding does not necessarily reject the former theories, as the definition of dust emissions may differ across studies. Another notable possibility is a shift in emission mechanisms with wind speed—under light winds, the detachment of fine particles from surfaces of soil aggregates dominates the emissions, generating more fine dust; in contrast, the fragmentation of soil aggregates dominates emissions under stronger winds and ejects more coarse dusts (Malinovskaya et al., 2021). The positive correlation between coarse dust fraction and slope is most pronounced under uphill winds. This aligns with the impacts of flow separation induced by topography, as suggested by previous numerical simulations (Heisel et al., 2021), but contradicts the observed effects of frontal winds explained by the microphysics of dust emissions (Malinovskaya et al., 2021). Our finding suggests that the topographic influence on transport over hundreds to thousands of meters may override the localized effects (increased generation of fine particles) from secondary aeolian structures at scales of centimeters to meters.~~ The persistent influence of slope on increasing ~~the~~ coarse fraction, ~~regardless of wind direction~~, might be related to meteorological ~~conditions~~ (e.g., ~~the~~ orographic wind channelling); ~~Rosenburg et al., 2014~~ and soil conditions (e.g., increased availability and ~~gravatational~~ ~~gravitational~~ mobility of coarser particles on hills); ~~Washington et al., 2006~~. ~~The effect of slope is most pronounced under uphill winds, highlighting the transport enhancement by topography over distances of hundreds to thousands of meters, which overrides the potential impact of local emission mechanisms at scales of centimeters to meters.~~ Including interaction terms in the model allows us to investigate shifts in the effects of wind conditions on dust size under different environmental conditions. The positive correlation between wind speed and coarse fraction diminishes during afternoon and summer events and under high soil moisture. This reduction is likely due to decreased differences in dust size distribution by deposition during haboob convective storms when turbulence is strong ~~(Heinold et al., 2013; Knippertz, 2017)~~. The uphill slope exhibits the strongest effect on increasing dust size in the morning, suggesting that the enhanced vertical transport is particularly effective in uplifting coarse dust during emissions related to the breakdown of night-time low-level jets ~~(Fiedler et al., 2015; Heinold et al., 2013)~~. The effect of uphill slope is weakened during summer and afternoons, indicating that turbulence during haboob dust storms has competing effects in sustaining airborne coarse dust.

This work provides insights into the controlling factors of dust PSD on a regional scale using a meta-analysis of a 10-year dust reanalysis dataset, ~~which~~ complementing the accumulating knowledge from recent field measurements. The study highlights the

580 overlapping effects and interactions among various environmental factors on the size distribution of dust emissions, which can
581 potentially be applied to improve dust emission parameterizations in regional to global Earth system models. Moreover, the
582 workflow for screening fresh dust events developed in this work serves as a reference for future studies utilizing datasets at various
583 scales. Remaining uncertainties in this work (e.g., those introduced by unmatched resolution of source data or lack of explicit
584 information on dust event types) and calls for ~~more~~ further investigation, work especially focusing on the role of different various
585 environmental factors and their interactions ~~at various scales~~. Additional field measurements, as well as the development and
586 validation of data products providing detailed information on size-resolved dust emissions, meteorological conditions, and soil and
587 topographic properties, would be crucial for advancing this field. Meanwhile, the workflow for screening fresh dust events
588 developed in this study will facilitate future work of utilizing datasets at different scales.

589

590

591 **Data Availability**

592 The open-access MONARCH dust reanalysis data, prepared by the Barcelona Supercomputing Center (BSC), are available at
593 https://earth.bsc.es/thredds_dustclim/homepage/. The Modern-Era Retrospective analysis for Research and Applications
594 (MERRA-2) data (Gelaro et al., 2017) are managed by the NASA Goddard Earth Sciences (GES) Data and Information Services
595 Center (DISC) and can be accessed at <https://disc.gsfc.nasa.gov/datasets?project=MERRA-2>. The NASA Shuttle Radar
596 Topography Mission Global 3 arc-second (SRTM GL3) dataset is available at <https://lpdaac.usgs.gov/products/srtmgl3v003/>. The
597 soil texture map input to the Global Land Data Assimilation System version 2 (GLDAS2) Noah land surface model (Rodell et al.,
598 2004) is described and provided by NASA at <https://ldas.gsfc.nasa.gov/gldas/soils>.

599

600 **Competing Interests**

601 The authors declare that they have no conflict of interests.

602

603 **Author Contribution**

604 HF secured funding for the research. HF and XH conceptualized the study, developed methodology for data collection and
605 processing, and provided the scientific interpretation of the results. XH processed the data and created the data visualizations. WG
606 conducted the statistical analysis of the processed data, drafted the corresponding methods (Section 2.4), and verified the initial
607 interpretation based on the statistical results. XH wrote the initial draft of the manuscript, and all authors contributed to the final
608 version.

609

610 **Acknowledgements**

611 This work was supported by the National Aeronautics and Space Administration (NASA) under Grant 80NSSC20K1532. We are
612 grateful to Dr. Clair Ryder for her guidance on the Fennec campaign data, and to Dr. Carlos Pérez García-Pando for reviewing the
613 manuscript and providing valuable insights into the interpretation of the results.

614

615 **References**

616 Adebiyi, A. A. and Kok, J. F.: Climate models miss most of the coarse dust in the atmosphere, *Science Advances*, 6,
617 doi:10.1126/sciadv.aaz9507, 2020.

618 Alfaro, S. C., Bouet, C., Khalfallah, B., Shao, Y., Ishizuka, M., Labiad, M., Marticorena, B., Laurent, B., and Rajot, J. L.:
619 Unraveling the Roles of Saltation Bombardment and Atmospheric Instability on Magnitude and Size Distribution of
620 Dust Emission Fluxes: Lessons From the JADE and WIND-O-V Experiments, *Journal of Geophysical Research: Atmospheres*, 127, doi:10.1029/2021jd035983, 2022.

622 Bacanin, N., Perisic, M., Jovanovic, G., Damaševičius, R., Stanisic, S., Simic, V., Zivkovic, M., and Stojic, A.: The
623 explainable potential of coupling hybridized metaheuristics, XGBoost, and SHAP in revealing toluene behavior in
624 the atmosphere, *Science of The Total Environment*, 929, 172195, doi:10.1016/j.scitotenv.2024.172195, 2024.

625 Berkson, J.: Application of the Logistic Function to Bio-Assay, *Journal of the American Statistical Association*, 39, 357–
626 365, doi:10.2307/2280041, 1944.

627 Box, G. E. P. and Cox, D. R.: An Analysis of Transformations, *Journal of the Royal Statistical Society Series B: Statistical*
628 *Methodology*, 26, 211–243, doi:10.1111/j.2517-6161.1964.tb00553.x, 1964.

629 Brasseur, G. P. and Jacob, D. J.: *Modeling of Atmospheric Chemistry*, Cambridge University Press, Cambridge,
630 doi:10.1017/9781316544754, 2017.

631 Brokamp, C., Jandarov, R., Rao, M. B., LeMasters, G., and Ryan, P.: Exposure assessment models for elemental
632 components of particulate matter in an urban environment: A comparison of regression and random forest
633 approaches, *Atmospheric Environment*, 151, 1–11, doi:10.1016/j.atmosenv.2016.11.066, 2017.

634 Caton Harrison, T., Washington, R., Engelstaedter, S., Jones, R. G., and Savage, N. H.: Influence of Orography Upon
635 Summertime Low-Level Jet Dust Emission in the Central and Western Sahara, *Journal of Geophysical Research: Atmospheres*, 126, doi:10.1029/2021jd035025, 2021.

637 Chen, T. and Guestrin, C.: XGBoost: A Scalable Tree Boosting System, *Proceedings of the 22nd ACM SIGKDD*
638 *International Conference on Knowledge Discovery and Data Mining*, San Francisco, California, USA,
639 doi:10.1145/2939672.2939785, 2016.

640 Chkhetiani, O. G., Vazaeva, N. V., Chernokulsky, A. V., Shukurov, K. A., Gubanova, D. P., Artamonova, M. S.,
641 Maksimenkov, L. O., Kozlov, F. A., and Kuderina, T. M.: Analysis of Mineral Aerosol in the Surface Layer over
642 the Caspian Lowland Desert by the Data of 12 Summer Field Campaigns in 2002–2020, *Atmosphere*, 12,
643 doi:10.3390/atmos12080985, 2021.

644 Cribari-Neto, F. and Zeileis, A.: Beta Regression in R, *Journal of Statistical Software*, 34, 1–24, doi:10.18637/jss.v034.i02,
645 2010.

646 Dee, D. P., Uppala, S., Simmons, A. J., Berrisford, P., Poli, P., Kobayashi, S., Andrae, U., Balmaseda, M., Balsamo, G.,
647 and Bauer, d. P.: The ERA-Interim reanalysis: Configuration and performance of the data assimilation system,
648 *Quarterly Journal of the royal meteorological society*, 137, 553–597, 2011.

649 Di Tomaso, E., Escribano, J., Basart, S., Ginoux, P., Macchia, F., Barnaba, F., Benincasa, F., Bretonnière, P. A., Buñuel,
650 A., Castrillo, M., Cuevas, E., Formenti, P., Gonçalves, M., Jorba, O., Klose, M., Mona, L., Montané Pinto, G.,
651 Mytilinaios, M., Obiso, V., Olid, M., Schutgens, N., Votsis, A., Werner, E., and Pérez García-Pando, C.: The
652 MONARCH high-resolution reanalysis of desert dust aerosol over Northern Africa, the Middle East and Europe
653 (2007–2016), *Earth System Science Data Syst. Sci. Data*, 14, 2785–2816, doi:10.5194/essd-14-2785-2022, 2022.

654 Douma, J. C. and Weedon, J. T.: Analysing continuous proportions in ecology and evolution: A practical introduction to
655 beta and Dirichlet regression, *Methods in Ecology and Evolution*, 10, 1412–1430, doi:10.1111/2041-210x.13234,
656 2019.

657 Duce, R. A. and Tindale, N. W.: Atmospheric transport of iron and its deposition in the ocean, *Limnology and
658 Oceanography*, 36, 1715–1726, doi:10.4319/lo.1991.36.8.1715, 1991.

659 Dupont, S.: On the Influence of Thermal Stratification on Emitted Dust Flux, *Journal of Geophysical Research: Atmospheres*, 127, doi:10.1029/2022jd037364, 2022.

660 Dupont, S., Alfaro, S. C., Bergametti, G., and Marticorena, B.: Near-surface dust flux enrichment in small particles during
661 erosion events, *Geophysical Research Letters*, 42, 1992–2000, doi:10.1002/2015gl063116, 2015.

662 Farr, T. G., Rosen, P. A., Caro, E., Crippen, R., Duren, R., Hensley, S., Kobrick, M., Paller, M., Rodriguez, E., Roth, L.,
663 Seal, D., Shaffer, S., Shimada, J., Umland, J., Werner, M., Oskin, M., Burbank, D., and Alsdorf, D.: The Shuttle
664 Radar Topography Mission, *Reviews of Geophysics*, 45, doi:10.1029/2005rg000183, 2007.

665 Fernandes, R., Dupont, S., and Lamaud, E.: Experimental evidence of dust flux size distribution variation along two
666 consecutive erosion seasons, *Aeolian Research*, 61, doi:10.1016/j.aeolia.2023.100863, 2023.

667 Fiedler, S., Kaplan, M. L., and Knippertz, P.: The importance of Harmattan surges for the emission of North African dust
668 aerosol, *Geophysical Research Letters*, 42, 9495–9504, doi:10.1002/2015gl065925, 2015.

669 Formenti, P., Schütz, L., Balkanski, Y., Desboeufs, K., Ebert, M., Kandler, K., Petzold, A., Scheuvens, D., Weinbruch, S.,
670 and Zhang, D.: Recent progress in understanding physical and chemical properties of African and Asian mineral
671 dust, *Atmospheric Chemistry and Physics*, 11, 8231–8256, doi:10.5194/acp-11-8231-2011, 2011.

672 Fox, J. and Weisberg, S.: *An R Companion to Applied Regression*, 2019.

673 Fujiwara, M., Martineau, P., Wright, J. S., Abalos, M., Šácha, P., Kawatani, Y., Davis, S. M., Birner, T., and Monge-Sanz,
674 B. M.: Climatology of the terms and variables of transformed Eulerian-mean (TEM) equations from multiple
675 reanalyses: MERRA-2, JRA-55, ERA-Interim, and CFSR, *Atmospheric Chemistry and Physics Atmos. Chem. Phys.*,
676 24, 7873–7898, doi:10.5194/acp-24-7873-2024, 2024.

677 Gelaro, R., McCarty, W., Suárez, M. J., Todling, R., Molod, A., Takacs, L., Randles, C. A., Darmenov, A., Bosilovich, M.
678 G., Reichle, R., Wargan, K., Coy, L., Cullather, R., Draper, C., Akella, S., Buchard, V., Conaty, A., da Silva, A. M.,

680 Gu, W., Kim, G.-K., Koster, R., Lucchesi, R., Merkova, D., Nielsen, J. E., Partyka, G., Pawson, S., Putman, W.,
681 Rienecker, M., Schubert, S. D., Sienkiewicz, M., and Zhao, B.: The Modern-Era Retrospective Analysis for Research
682 and Applications, Version 2 (MERRA-2), *Journal of Climate*, 30, 5419–5454, doi:10.1175/JCLI-D-16-0758.1,
683 2017.

684 Gesch, D., Williams, J., and Miller, W.: A comparison of US geological survey seamless elevation models with shuttle
685 radar topography mission data, *IGARSS 2001. Scanning the Present and Resolving the Future. Proceedings. IEEE*
686 2001 *International Geoscience and Remote Sensing Symposium* (Cat. No. 01CH37217), 754–756, 2001.

687 Ginoux, P., Chin, M., Tegen, I., Prospero, J. M., Holben, B., Dubovik, O., and Lin, S.-J.: Sources and distributions of dust
688 aerosols simulated with the GOCART model, *Journal of Geophysical Research: Atmospheres*, 106, 20255 –20273,
689 doi:10.1029/2000JD000053, 2001.

690 Ginoux, P., Prospero, J. M., Gill, T. E., Hsu, N. C., and Zhao, M: Global-scale attribution of anthropogenic and natural
691 dust sources and their emission rates based on MODIS Deep Blue aerosol products, *Reviews of Geophysics* Rev.
692 *Geophys.*, 50, RG3005, doi:10.1029/2012RG000388, 2012.

693 González-Flórez, C., Klose, M., Alastuey, A., Dupont, S., Escribano, J., Etyemezian, V., Gonzalez-Romero, A., Huang, Y.,
694 Kandler, K., Nikolic, G., Panta, A., Querol, X., Reche, C., Yus-Díez, J., and Pérez García-Pando, C.: Insights into
695 the size-resolved dust emission from field measurements in the Moroccan Sahara, *Atmospheric Chemistry and*
696 *Physics* *Atmos. Chem. Phys.*, 23, 7177–7212, doi:10.5194/acp-23-7177-2023, 2023.

697 Graesser, J.: GeoWombat: Utilities for geospatial data [code], <https://github.com/jgrss/geowombat>, 2023.

698 Grün, B., Kosmidis, I., and Zeileis, A.: Extended Beta Regression in R: Shaken, Stirred, Mixed, and Partitioned, *Journal of*
699 *Statistical Software*, 48, 1–25, doi:10.18637/jss.v048.i11, 2012.

700 Heinold, B., Knippertz, P., Marsham, J. H., Fiedler, S., Dixon, N. S., Schepanski, K., Laurent, B., and Tegen, I.: The role
701 of deep convection and nocturnal low-level jets for dust emission in summertime West Africa: Estimates from
702 convection-permitting simulations, *Journal of Geophysical Research: Atmospheres* J. Geophys. Res. Atmos., 118,
703 4385–4400, doi:10.1002/jgrd.50402, 2013.

704 Heisel, M., Chen, B., Kok, J. F., and Chamecki, M.: Gentle Topography Increases Vertical Transport of Coarse Dust by
705 Orders of Magnitude, *Journal of Geophysical Research: Atmospheres*, 126, doi:10.1029/2021JD034564, 2021.

706 Ishizuka, M., Mikami, M., Leys, J., Yamada, Y., Heidenreich, S., Shao, Y., and McTainsh, G. H.: Effects of soil moisture
707 and dried raindrop crust on saltation and dust emission, *Journal of Geophysical Research: Atmospheres*, 113,
708 doi:10.1029/2008jd009955, 2008.

709 Jahn, R., Blume, H. P., Asio, V., Spaargaren, O., and Schád, P.: FAO Guidelines for Soil Description, 2006.

710 Katra, I.: Soil Erosion by Wind and Dust Emission in Semi-Arid Soils Due to Agricultural Activities, *Agronomy*, 10,
711 doi:10.3390/agronomy10010089, 2020.

712 Keller, C. A. and Evans, M. J.: Application of random forest regression to the calculation of gas-phase chemistry within the
713 GEOS-Chem chemistry model v10, *Geoscientific Model Development* Geosci. Model. Dev., 12, 1209–1225,
714 10.5194/gmd-12-1209-2019, 2019.

715 Kellogg, C. A. and Griffin, D. W.: Aerobiology and the global transport of desert dust, *Trends in Ecology & Evolution* [Ecol. Evol.](#), 21, 638–644, doi:10.1016/j.tree.2006.07.004, 2006.

716

717 Khalfallah, B., Bouet, C., Labiad, M. T., Alfaro, S. C., Bergametti, G., Marticorena, B., Lafon, S., Chevaillier, S., Féron, A., Hease, P., Henry des Tureaux, T., Sekrafi, S., Zapf, P., and Rajot, J. L.: Influence of Atmospheric Stability on 718 the Size Distribution of the Vertical Dust Flux Measured in Eroding Conditions Over a Flat Bare Sandy Field, 719 *Journal of Geophysical Research: Atmospheres*, 125, doi:10.1029/2019jd031185, 2020.

720

721 Kiers, H. A. L.: Weighted least squares fitting using ordinary least squares algorithms, *Psychometrika*, 62, 251–266, 1997.

722

723 Klose, M., Jorba, O., Gonçalves Ageitos, M., Escribano, J., Dawson, M. L., Obiso, V., Di Tomaso, E., Basart, S., Montané Pinto, G., Macchia, F., Ginoux, P., Guerschman, J., Prigent, C., Huang, Y., Kok, J. F., Miller, R. L., and Pérez 724 García-Pando, C.: Mineral dust cycle in the Multiscale Online Nonhydrostatic AtmosphéRe CHEmistry model 725 (MONARCH) Version 2.0, [Geoscientific Model Development](#) [Geosci. Model Dev.](#), 14, 6403–6444, 726 doi:10.5194/gmd-14-6403-2021, 2021.

727

728 Knippertz, P.: Mineral Dust Generation across Northern Africa and Its Impacts, [in](#) Oxford Research Encyclopedia of Climate Science, doi:10.1093/acrefore/9780190228620.013.516, 2017.

729

730 Knippertz, P., Deutscher, C., Kandler, K., Müller, T., Schulz, O., and Schütz, L.: Dust mobilization due to density currents 731 in the Atlas region: Observations from the Saharan Mineral Dust Experiment 2006 field campaign, *Journal of Geophysical Research: Atmospheres*, 112, doi:10.1029/2007jd008774, 2007.

732

733 Kok, J. F.: Does the size distribution of mineral dust aerosols depend on the wind speed at emission?, *Atmospheric Chemistry and Physics*, 11, 10149–10156, doi:10.5194/acp-11-10149-2011, 2011.

734

735 Kok, J. F., Parteli, E. J. R., Michaels, T. I., and Karam, D. B.: The physics of wind-blown sand and dust, *Reports on Progress in Physics*, 75, 106901, doi:10.1088/0034-4885/75/10/106901, 2012.

736

737 Kok, J. F., Albani, S., Mahowald, N. M., and Ward, D. S.: An improved dust emission model – Part 2: Evaluation in the 738 Community Earth System Model, with implications for the use of dust source functions, [Atmospheric Chemistry and Physics](#) [Atmos. Chem. Phys.](#), 14, 13043 –13061, doi:10.5194/acp-14-13043-2014, 2014.

739

740 Kok, J. F., Storelvmo, T., Karydis, V. A., Adebiyi, A. A., Mahowald, N. M., Evan, A. T., He, C., and Leung, D. M.: Mineral 741 dust aerosol impacts on global climate and climate change, *Nature Reviews Earth & Environment*, 4, 71–86, doi:10.1038/s43017-022-00379-5, 2023.

742

743 Lu, S., Symonds, P., Verschoor, N., Chalabi, Z., Taylor, J., and Davies, M.: Use of Beta Regression to investigate the link 744 between home air infiltration rate and self-reported health, *Journal of Physics: Conference Series*, 2069, doi:10.1088/1742-6596/2069/1/012178, 2021.

745

746 Lundberg, S. M. and Lee, S.-I.: A unified approach to interpreting model predictions, *Proceedings of the 31st International Conference on Neural Information Processing Systems*, Long Beach, California, USA, 2017.

747

748 Ma, X., Gao, Q., Jiang, X., Chen, S., Gan, Y., Zhang, T., Lu, X., and Wang, X.: Direct Effects of Air Humidity on Dust 749 Aerosol Production: Evidences for the Surprising Role of Electrostatic Forces, *Geophysical Research Letters*, 50, doi:10.1029/2023gl103639, 2023.

750 Mahowald, N., Albani, S., Kok, J. F., Engelstaeder, S., Scanza, R., Ward, D. S., and Flanner, M. G.: The size distribution
751 of desert dust aerosols and its impact on the Earth system, *Aeolian Research*, 15, 53–71,
752 doi:10.1016/j.aeolia.2013.09.002, 2014.

753 Malinovskaya, E. A., Chkhetiani, O. G., and Maksimenkov, L. O.: Influence of Wind Direction on the Size Distribution of
754 Aeolian Microparticles, *Izvestiya, Atmospheric and Oceanic Physics*, 57, 472–485,
755 doi:10.1134/S0001433821050108, 2021.

756 Marticorena, B. and Bergametti, G.: Modeling the atmospheric dust cycle: 1. Design of a soil-derived dust emission scheme,
757 *Journal of Geophysical Research geophysical research: Atmospheres*, 100, 16415–16430, 1995.

758 Meng, J., Huang, Y., Leung, D. M., Li, L., Adebiyi, A. A., Ryder, C. L., Mahowald, N. M., and Kok, J. F.: Improved
759 Parameterization for the Size Distribution of Emitted Dust Aerosols Reduces Model Underestimation of Super
760 Coarse Dust, *Geophysical Research Letters*, 49, doi:10.1029/2021GL097287, 2022.

761 Mytilinaios, M., Basart, S., Ciamprone, S., Cuesta, J., Dema, C., Di Tomaso, E., Formenti, P., Gkikas, A., Jorba, O., Kahn,
762 R., Pérez García-Pando, C., Trippetta, S., and Mona, L.: Comparison of dust optical depth from multi-sensor
763 products and MONARCH (Multiscale Online Non-hydrostatic AtmospheRe CHemistry) dust reanalysis over North
764 Africa, the Middle East, and Europe, *Atmospheric Chemistry and Physics*, 23, 5487–5516,
765 doi:10.5194/acp-23-5487-2023, 2023.

766 Panebianco, J. E., Avecilla, F., Funk, R., and Buschiazza, D. E.: Influence of friction velocity and saltation intensity on the
767 particle-size distribution of dust (PM32) emitted from an agricultural soil, *Earth Surface Processes and Landforms*,
768 48, 1176–1187, doi:10.1002/esp.5541, 2023.

769 Pedregosa, F., Varoquaux, G., Gramfort, A., Michel, V., Thirion, B., Grisel, O., Blondel, M., Prettenhofer, P., Weiss, R.,
770 Dubourg, V., Vanderplas, J., Passos, A., Cournapeau, D., Brucher, M., Perrot, M., and Duchesnay, É.: Scikit-learn:
771 Machine Learning in Python, *Journal of Machine Learning Research J. Mach. Learn. Res.*, 12, 2825–2830, 2011.

772 Peleg, M.: Beta distributions for particle size having a finite range and predetermined mode, mean or median, *Powder
773 Technology*, 356, 790–794, doi:10.1016/j.powtec.2019.09.015, 2019.

774 Polymenakou, P. N., Mandalakis, M., Stephanou, E. G., and Tselepides, A.: Particle size distribution of airborne
775 microorganisms and pathogens during an Intense African dust event in the eastern Mediterranean, *Environmental
776 Health Perspectives*, 116, 292–296, doi:10.1289/ehp.10684, 2008.

777 Prospero, J. M., Blades, E., Mathison, G., and Naidu, R.: Interhemispheric transport of viable fungi and bacteria from Africa
778 to the Caribbean with soil dust, *Aerobiologia*, 21, 1–19, doi:10.1007/s10453-004-5872-7, 2005.

779 Pu, B., and Ginoux, P.: The impact of the Pacific Decadal Oscillation on springtime dust activity in Syria, *Atmospheric
780 Chemistry and Physics*, 16, 13431–13448, doi:10.5194/acp-16-13431-2016, 2016.

781 R. Core Team: R: A Language and Environment for Statistical Computing, 2023.

782 Reynolds, C. A., Jackson, T. J., and Rawls, W. J.: Estimating soil water-holding capacities by linking the Food and
783 Agriculture Organization Soil map of the world with global pedon databases and continuous pedotransfer functions,
784 *Water Resources Research*, 36, 3653–3662, doi:10.1029/2000wr900130, 2000.

785 Rienecker, M. M., Suarez, M., Todling, R., Bacmeister, J., Takacs, L., Liu, H.-C., Gu, W., Sienkiewicz, M., Koster, R., and
786 Gelaro, R.: The GEOS-5 Data Assimilation System-Documentation of Versions 5.0. 1, 5.1. 0, and 5.2. 0, 2008.

787 Rodell, M., Houser, P. R., Jambor, U., Gottschalck, J., Mitchell, K., Meng, C. J., Arsenault, K., Cosgrove, B., Radakovich,
788 J., Bosilovich, M., Entin*, J. K., Walker, J. P., Lohmann, D., and Toll, D.: The Global Land Data Assimilation
789 System, *Bulletin of the American Meteorological Society*, 85, 381–394, doi:10.1175/BAMS-85-3-381, 2004.

790 Rosenberg, P. D., Parker, D. J., Ryder, C. L., Marsham, J. H., Garcia-Carreras, L., Dorsey, J. R., Brooks, I. M., Dean, A.
791 R., Crosier, J., McQuaid, J. B., and Washington, R.: Quantifying particle size and turbulent scale dependence of dust
792 flux in the Sahara using aircraft measurements, *Journal of Geophysical Research: Atmospheres*, 119, 7577–7598,
793 doi:10.1002/2013jd021255, 2014.

794 Ryder, C. L.: Radiative Effects of Increased Water Vapor in the Upper Saharan Air Layer Associated With Enhanced
795 Dustiness, *Journal of Geophysical Research: Atmospheres*, 126, doi:10.1029/2021jd034696, 2021.

796 Ryder, C. L., Highwood, E. J., Walser, A., Seibert, P., Philipp, A., and Weinzierl, B.: Coarse and giant particles are
797 ubiquitous in Saharan dust export regions and are radiatively significant over the Sahara, *Atmospheric Chemistry*
798 and *Physics*, 19, 15353–15376, doi:10.5194/acp-19-15353-2019, 2019.

799 Ryder, C. L., Highwood, E. J., Rosenberg, P. D., Trembath, J., Brooke, J. K., Bart, M., Dean, A., Crosier, J., Dorsey, J.,
800 Brindley, H., Banks, J., Marsham, J. H., McQuaid, J. B., Sodemann, H., and Washington, R.: Optical properties of
801 Saharan dust aerosol and contribution from the coarse mode as measured during the Fennec 2011 aircraft campaign,
802 *Atmospheric Chemistry and Physics*, 13, 303–325, doi:10.5194/acp-13-303-2013, 2013.

803 Ryder, C. L., McQuaid, J. B., Flamant, C., Rosenberg, P. D., Washington, R., Brindley, H. E., Highwood, E. J., Marsham,
804 J. H., Parker, D. J., Todd, M. C., Banks, J. R., Brooke, J. K., Engelstaedter, S., Estelles, V., Formenti, P., Garcia-
805 Carreras, L., Kocha, C., Marenco, F., Sodemann, H., Allen, C. J. T., Bourdon, A., Bart, M., Cavazos-Guerra, C.,
806 Chevaillier, S., Crosier, J., Derbyshire, E., Dean, A. R., Dorsey, J. R., Kent, J., O'Sullivan, D., Schepanski, K., Szpek,
807 K., Trembath, J., and Woolley, A.: Advances in understanding mineral dust and boundary layer processes over the
808 Sahara from Fennec aircraft observations, *Atmospheric Chemistry and Physics*, 15, 8479–8520, doi:10.5194/acp-
809 15-8479-2015, 2015.

810 Samuel-Rosa, A., Dalmolin, R. S. D., and Miguel, P.: Building predictive models of soil particle-size distribution, *Revista*
811 *Brasileira de Ciência do Solo*, 37, 422–430, doi:10.1590/s0100-06832013000200013, 2013.

812 Santos, J., Sakagami, Y., Haas, R., Passos, J., Machuca, M., Radünz, W., Dias, E., and Lima, M.: Wind speed evaluation
813 of MERRA-2, ERA-interim and ERA-5 reanalysis data at a wind farm located in brazil, *Proceedings of the ISES*
814 *Solar World Congress*, 1–10, 2019.

815 Shao, Y.: A model for mineral dust emission, *Journal of Geophysical Research: Atmospheres*, 106, 20239–20254,
816 doi:10.1029/2001jd900171, 2001.

817 Shao, Y., Zhang, J., Ishizuka, M., Mikami, M., Leys, J., and Huang, N.: Dependency of particle size distribution at dust
818 emission on friction velocity and atmospheric boundary-layer stability, *Atmospheric Chemistry and Physics*, 20,
819 12939–12953, doi:10.5194/acp-20-12939-2020, 2020.

820 Tanaka, T. Y. and Chiba, M.: A numerical study of the contributions of dust source regions to the global dust budget, *Global*
821 and *Planetary Change*, 52, 88–104, doi:10.1016/j.gloplacha.2006.02.002, 2006.

822 Venables, W. N. and Ripley, B. D.: *Modern Applied Statistics with S*, 2002.

823 Wang, R., Li, Q., Wang, R., Chang, C., Guo, Z., Li, J., and Zhou, N.: Influence of Wind Velocity and Soil Size Distribution
824 on Emitted Dust Size Distribution: A Wind Tunnel Study, *Journal of Geophysical Research: Atmospheres*, 126,
825 doi:10.1029/2020jd033768, 2021.

826 Wang, X., Wang, Q., Prass, M., Pöhlker, C., Moran-Zuloaga, D., Artaxo, P., Gu, J., Yang, N., Yang, X., Tao, J., Hong, J.,
827 Ma, N., Cheng, Y., Su, H., and Andreae, M. O.: The export of African mineral dust across the Atlantic and its impact
828 over the Amazon Basin, *Atmospheric Chemistry and Physics*, 23, 9993–10014, doi:10.5194/acp-23-9993-2023,
829 2023.

830 Washington, R., Todd, M. C., Lizcano, G., Tegen, I., Flamant, C., Koren, I., Ginoux, P., Engelstaedter, S., Bristow, C. S.,
831 Zender, C. S., Goudie, A. S., Warren, A., and Prospero, J. M.: Links between topography, wind, deflation, lakes and
832 dust: The case of the Bodélé Depression, *Chad*, *Geophysical Research Letters*, 33, doi:10.1029/2006gl025827, 2006.

833 Webb, N. P., LeGrand, S. L., Cooper, B. F., Courtright, E. M., Edwards, B. L., Felt, C., Van Zee, J. W., and Ziegler, N. P.:
834 Size Distribution of Mineral Dust Emissions From Sparsely Vegetated and Supply-Limited Dryland Soils, *Journal*
835 of *Geophysical Research: Atmospheres*, 126, doi:10.1029/2021jd035478, 2021.

836 Yamaguchi, N., Ichijo, T., Sakotani, A., Baba, T., and Nasu, M.: Global dispersion of bacterial cells on Asian dust, *Scientific*
837 *Reports*, 2, 525, doi:10.1038/srep00525, 2012.

838 Zeileis, A. and Hothorn, T.: Diagnostic Checking in Regression Relationships, *R News*, 2, 7–10, 2002.

839 Zhang, B., Zhang, Y., and Jiang, X.: Feature selection for global tropospheric ozone prediction based on the BO-XGBoost-
840 RFE algorithm, *Scientific Reports*, 12, 9244, doi:10.1038/s41598-022-13498-2, 2022.

841 Zhuang, J., Dussin, R., Huard, D., Bourgault, P., Banihirwe, A., Raynaud, S., Malevich, B., Schupfner, M., Filipe, Levang,
842 S., Jüling, A., Almansi, M., RichardScottOz, RondeauG, Rasp, S., Smith, T. J., Stachelek, J., Plough, M., Pierre,
843 Bell, R., and Li, X.: pangeo-data/xESMF: v0.7.1 (v0.7.1), Zenodo [code], doi:10.5281/zenodo.7800141, 2023.